



A Lagrangian Analysis of Pockets of Open Cells over the Southeast Pacific

Kevin M. Smalley¹, Matthew D. Lebsock¹, Ryan Eastman², Mark Smalley^{1,3}, and Mikael K. Witte^{1,3,4}

¹Jet Propulsion Laboratory, California Institute of Technology, Pasadena, California, USA

²Department of Atmospheric Sciences, University of Washington, Seattle, Washington

³Joint Institute for Regional Earth System Science and Engineering, University of California, Los Angeles, California

⁴Naval Postgraduate School, Meteorology, Monterey, California, USA

Correspondence: Kevin M. Smalley (ksmalley@jpl.nasa.gov)

Abstract. Pockets of open cells (POCs) have been shown to develop within closed-cell stratocumulus (StCu) and a large body of evidence suggests that the development of POCs result from changes in small-scale processes internal to the boundary layer rather than large-scale forcings. Precipitation is widely viewed as a key process important to POC development and maintenance. In this study, GOES-16 satellite observations are used in conjunction with MERRA-2 winds to track and compare the microphysical and environmental evolution of two populations of closed-cell StCu selected by visual inspection over the southeast Pacific Ocean: one group that transitions to POCs and another control group that does not. The high spatio-temporal resolution of the new GOES-16 data allows for a detailed examination of the temporal evolution of POCs in this region. We find that POCs tend to develop near the coast, last tens of hours, are larger than 104 km², and often (88% of cases) do not re-close before they exit the StCu deck. Most POCs are observed to form at night and tend to exit the StCu during the day when the StCu is contracting in area. Relative to the control trajectories, POCs have systematically larger effective radii, lower cloud drop number concentrations, comparable conditional in-cloud liquid water path, and a higher frequency of more intense rainfall. Meanwhile, no systematic environmental differences other than boundary-layer height are observed between POC and control trajectories. These results support the consensus view regarding the importance of precipitation on the formation and maintenance of POCs and demonstrate the utility of modern geostationary remote sensing data in evaluating POC lifecycle.

1 Introduction

Stratocumulus (StCu) often organize into two distinct regimes: closed and open cells. Closed cells tend to have a higher albedo (McCoy et al., 2017) and greater cloud fraction (CF; Rosenfeld et al., 2006) than open cells, while open cells tend to produce more intense precipitation, especially at the edge of open cells (Stevens et al., 2005; Wood et al., 2008, 2011; Eastman et al., 2019; Sarkar et al., 2019). It is commonly observed that regions of open cells can develop within closed-cell Sc, and these regions have been defined as pockets of open cells (POCs; Bretherton et al., 2004; Stevens et al., 2005). POCs are often long-lived (10s of hours to a few days) once they have formed (e.g. Stevens et al., 2005; Berner et al., 2013).

A large body of evidence suggests that POCs are subject to a similar large-scale environment as closed-cell StCu that never transition to open cells. For example, several studies have found that the inversion height within POCs is similar to the nearby



25 closed-cell region (Sharon et al., 2006; Bretherton et al., 2010; Berner et al., 2011, 2013). Sharon et al. (2006) used aircraft
observations from the Drizzle and Entrainment Cloud Study coupled with GOES-10 geostationary observations to analyze the
characteristics of rifts of open cells embedded within the StCu deck. They found that the boundary layer within both the rift and
surrounding cloud is well-mixed with similar moisture profiles above the boundary layer. Using a mixed-layer model and large-
eddy simulations (LES), (Bretherton et al., 2010) hypothesized that POCs and the surrounding StCu have inversion heights that
are 'symbiotically' locked together through dynamical coupling even though the two adjacent regions may experience different
30 local cloud-top entrainment rates. Studies have also noted that POCs tend to be advected by the mean flow (i.e., same direction
and at the same speed) along with the surrounding StCu (Stevens et al., 2005; Sharon et al., 2006; Comstock et al., 2007) and
in-situ data indicates that wind shear within the POCs and the surrounding cloud are similar (Comstock et al., 2007). Taken
together, the observations and theory indicate that transitions of closed-cell StCu to POCs are not driven by differences in
large-scale meteorological forcing but are instead driven by processes internal to the boundary layer.

35 Precipitation is widely viewed as a key process in the development and maintenance of POCs. Prior observationally-based
studies have found that POCs form at night (Wood et al., 2011; Burleyson et al., 2013; Burleyson and Yuter, 2015) when the
most intense precipitation in the closed-cell stratocumulus deck begins to cluster and organize (Comstock et al., 2007; Savic-
Jovicic and Stevens, 2008; Wang et al., 2010a; Glassmeier and Feingold, 2017). In response, cold pools develop that drive more
intense updrafts and precipitation (Wang and Feingold, 2009; Terai and Wood, 2013; Yamaguchi and Feingold, 2015; Ghate
40 et al., 2020), especially at the boundary between open and closed cells (Stevens et al., 2005; Wood et al., 2008), which act to
both reduce CF by depleting cloud water (Austin et al., 1995) and drive the entrainment of drier air at cloud top (Comstock
et al., 2005). Observational studies have also found the air inside POCs tends to have lower aerosol concentrations (Petters
et al., 2006; Szoeké et al., 2009; Wang and Feingold, 2009; Wood et al., 2011; Terai et al., 2014), which results in a more
conducive environment for precipitation by reducing the number of cloud droplets while increasing their size (Wood et al.,
45 2011; Abel et al., 2017; Watson-Parris et al., 2021). Feingold et al. (2015) used a cloud-resolving model to show that aerosol
concentrations in the cloud layer are especially important for the end of a POC's lifetime. They found that there needs to be
an injection of aerosols into the POC which can allow the generation of cloud water to overcome precipitation loss causing the
POC to close, which can be achieved through events like biomass burning (Abel et al., 2020; Gupta et al., 2021).

To perform a process-based analysis of POC transitions, a model is needed. However, observations can be used to infer
50 processes influencing POCs such as precipitation by analyzing the differences in cloud microphysical properties between
POC regions and the surrounding closed-cell clouds. Prior observational-based studies have primarily used field-campaign
observations to analyze POCs (e.g. Petters et al., 2006; Szoeké et al., 2009; Wood et al., 2011; Terai et al., 2014). Most
satellite-based studies have primarily focused on differences between closed- and open-cell StCu (e.g. Painemal and Zuidema,
2010; Goren et al., 2018; Eastman et al., 2021), but a few have focused on the characteristics of POCs and the surrounding Sc.
55 Of note, Wood et al. (2008) used a combination of shipborne remote sensing coupled with MODIS and GOES-8 observations
to analyze changes in cloud drop number concentration and liquid water path within POCs, finding that POCs tend to form in
regions of higher liquid water path and lower number concentrations. Recently, Watson-Parris et al. (2021) composited MODIS



observations of POCs between 2005 and 2018 to analyze POC characteristics. They found POCs have a larger effective radius, lower cloud optical depth, and smaller cloud water path than the surrounding cloud.

60 A foundational aspect of Wood et al. (2008) was their use of GOES-8 to investigate POC development. By using geosynchronous observations, they were not limited to instantaneous snapshots of POCs from instruments such as MODIS (e.g. Eastman and Wood, 2016; Watson-Parris et al., 2021). Wood et al. (2008) found that two-thirds of the POC cases identified between September and October 2001 formed in the early morning hours when cloud drop and aerosol concentrations were lowest. However, the cloud microphysical characteristics were not derived from GOES-8; instead, Wood et al. (2008) 65 qualitatively compared the GOES-8 visible, near-infrared, and infrared observations to MODIS-derived retrievals and aircraft observations. Abel et al. (2020) made quantitative use of the Spinning Enhanced Visible and Infrared Imager (Aminou, 2002) onboard the Meteosat Second Generation geosynchronous satellites and MODIS to investigate the influence of biomass burning on POCs. They found that the boundary layer within POCs is ultra-clean even in columns containing aerosols emitted from biomass burning, suggesting that open-cellular convection does not efficiently entrain free-tropospheric aerosols from 70 immediately above the inversion into the boundary layer.

In this study, we add a Lagrangian perspective of the full POC lifecycle from satellites by using GOES-16 passive measurements of StCu in the southeast Pacific (SEPAC). GOES-16 makes full-disk observations at 10-minute time intervals with a horizontal resolution between 0.5-2 km. The continuous observations afforded by a geostationary orbit allow for a characterization of POC cloud properties throughout the POC lifetime. Furthermore, the data allow for a comparison of the cloud 75 properties along Lagrangian trajectories that develop into POCs with similar trajectories that remain closed-cell. We use these observations to demonstrate that POCs and closed-cell StCu experience indistinguishable large-scale forcing yet markedly different cloud microphysical properties, thereby supporting the consensus view regarding the role of precipitation in POC formation and maintenance.

2 Data and Methods

80 2.1 POC Identification

We identify POCs visually by creating true-color RGBs using 0.47- μm , 0.64- μm , and 0.86- μm reflectance during the day and 10.3- μm – 3.9- μm brightness temperature difference ($\text{TB}_{10.3\mu\text{m}-3.9\mu\text{m}}$) images at night using Satpy (Raspaud et al., 2018) from 10-minute observations of GOES-16 ABI top-of-atmosphere solar reflectance and infrared brightness temperatures (IR; Schmit et al., 2017). The 0.64- μm reflectance is sampled at 0.5 km, while 0.47- μm and 0.86- μm reflectances are sampled at 1 85 km so we resample the 0.64 μm reflectance to 1 km resolution before creating the true-color RGBs. The 3.9- μm and 10.3- μm TBs are sampled at 2 km. We focus on the southeastern Pacific Ocean (SEPAC) defined as the region spanning 45°S – 5°N and 70°W – 120°W during September – November of 2019, and we create weekly animations of the true-color RGBs and $\text{TB}_{10.3\mu\text{m}-3.9\mu\text{m}}$ images to visually identify POCs. For consistency, we classify any region of clearing completely enclosed within the StCu deck as a POC with the following conditions: 1) regions of clearing at the StCu edge that become completely 90 enclosed within the StCu deck are not classified as POCs, and 2) any potential POCs that appear to develop in response to



gravity waves (Allen et al., 2013) are not included. This visual identification method is admittedly subjective, and the overall classification of POCs under this framework may slightly differ by person. However, our overall results, as discussed later, are consistent with prior POC studies and a subjective approach is common in this literature (e.g. Wood et al., 2008, 2011; Terai et al., 2014; Watson-Parris et al., 2021).

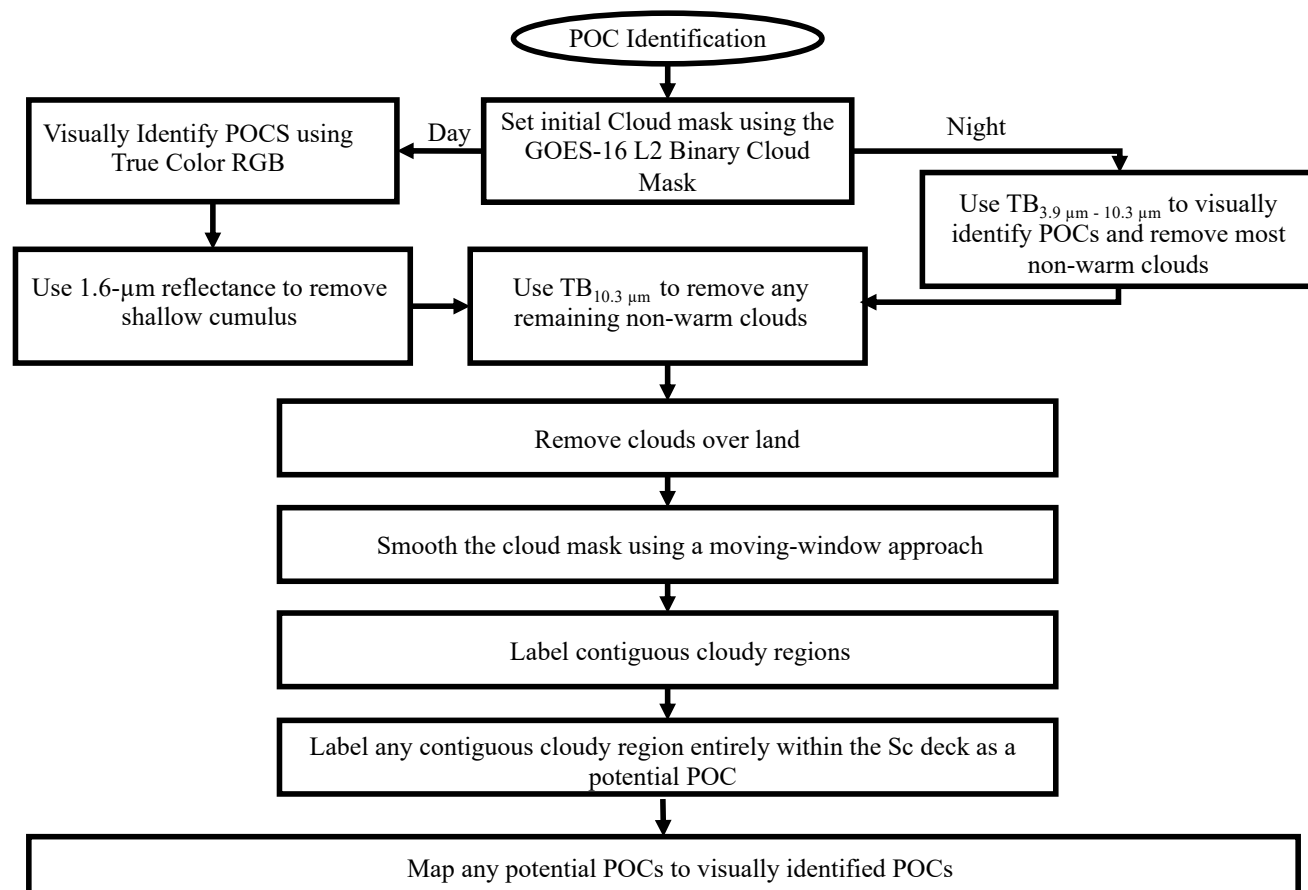


Figure 1. Flowchart of how POCs are identified.

95 Once we visually identify POCs, we develop an overcast-Sc mask that is used to track the evolution of each POC within the larger cloud field. As shown in Figure 1, the initial overcast-Sc mask is defined using the clear-sky mask level-2 product from GOES-16 by filtering out clear pixels (Heidinger and Straka, 2012). The next step is different depending on if there is daylight. During the day, 1.6- μm reflectance ($R_{1.6}$) (resampled from 1 km to 2 km) is used to filter out ice-phase clouds and many shallow cumulus clouds from the overcast-Sc mask. $R_{1.6}$ has two useful tendencies in this regard. First, because water



100 droplets are more reflective at $1.6\text{-}\mu\text{m}$ (Miller et al., 2014), $R_{1.6}$ tends to be larger for water droplets than ice crystals. Second, $R_{1.6}$ tends to be brighter in StCu than cumulus pixels (e.g. Zinner and Mayer, 2006; Wolters et al., 2010). To exploit these tendencies, we find the median $R_{1.6}$ of all cloudy pixels within the SEPAC region and exclude the lowest 50% of remaining cloud pixels that tend to be associated with ice-phase and liquid phase cumulus clouds (Figure 2c-d). At night, the initial filter uses $TB_{10.3\mu\text{m}\sim 3.9\mu\text{m}}$ as an initial overcast-Sc mask filter. Considering that warm cloud emissivity is smaller at $3.9\text{-}\mu\text{m}$ than
105 ice cloud emissivity but similar at $10.3\text{-}\mu\text{m}$ (Hunt, 1973), $TB_{10.3\mu\text{m}\sim 3.9\mu\text{m}}$ has been used to separate both cloud types (e.g. Jedlovec et al., 2008). Therefore, any pixels with $TB_{10.3\mu\text{m}\sim 3.9\mu\text{m}} < 0.3$ K are excluded (Figures 3c-d). Once the overcast-Sc mask is conditioned using either $R_{1.6}$ or $TB_{10.3\mu\text{m}\sim 3.9\mu\text{m}}$, we remove any remaining cold clouds using a threshold $10.3\text{-}\mu\text{m}$ TB of 273 K and clouds over land using the Global 1-km Base Elevation dataset (Hastings and Dunbar, 1999).

The filters above effectively precondition the overcast-Sc mask but it still likely includes the brightest shallow Cu and it can
110 be noisy near the edge of the StCu deck. To smooth the overcast-Sc mask, we calculate the mean binary mask value within a 25×25 pixel window centered on each pixel. We filter out any overcast-Sc mask pixels with a window-mean mask value < 0.5 (Figures 2i-j and 3i-j). We chose this threshold because, upon visual inspection, it does not over-smooth the overcast-Sc mask by removing the edge of POCs that are close to the StCu edge but does effectively remove large and bright shallow Cu.

From Figures 2i-j and 3i-j, we see that there are clear/variable cloudy regions within the overcast-Sc. Therefore, any con-
115 tiguous clear/variable cloudy region completely enclosed within a contiguous overcast region is classified as a potential POC (Figures 2k and 3k). We then map the potential POCs to the observed cloud field to visually confirm if a potential POC is meeting our subjective POC criteria defined above. Comparing Figure 2a to 2l and Figure 3a to 3l, we see that our algorithm can effectively identify both StCu decks and the POCs they enclose. We identify a total of 258 POCs over the study period.

2.2 Defining Lagrangian Trajectories

120 We use trajectory analysis to track the evolution of each POC. We define the initial POC time by identifying a time when each POC is larger than 3136 km^2 (approximately one $0.5^\circ\times 0.5^\circ$ gridbox) and visually not too irregularly shaped such that the POC centroid is contained within the POC region and not in the surrounding StCu. From this time and location, we run forward and backward trajectories using the nearest 3-hourly 925-mb horizontal winds from Modern-Era Retrospective analysis for Research and Applications, Version 2 (MERRA-2; Gelaro et al., 2017), with a time step of 10 minutes to follow
125 the Lagrangian evolution of POCs. The trajectories are run forward and backward from the initial time up to 6 hours before POC development or after POC dissipation. If any trajectory intersects any other POC in the 6-hour timeframe before POC development or after POC dissipation, it is terminated prematurely.

We classify the POC start time as the time along each trajectory when CF begins to decrease. POC end time is determined using two separate criteria: 1) CF increases back to 100% and does not change for more than an hour (hereby known as the
130 POCs that re-close) or 2) at least one POC edge reaches the edge of the StCu deck (hereby known as the POCs that never re-close). The first criterion is based on the calculated changes in CF along each trajectory, while the second criterion must be satisfied visually. Throughout the rest of the paper, these trajectories will be labeled as POC cases/trajectories.

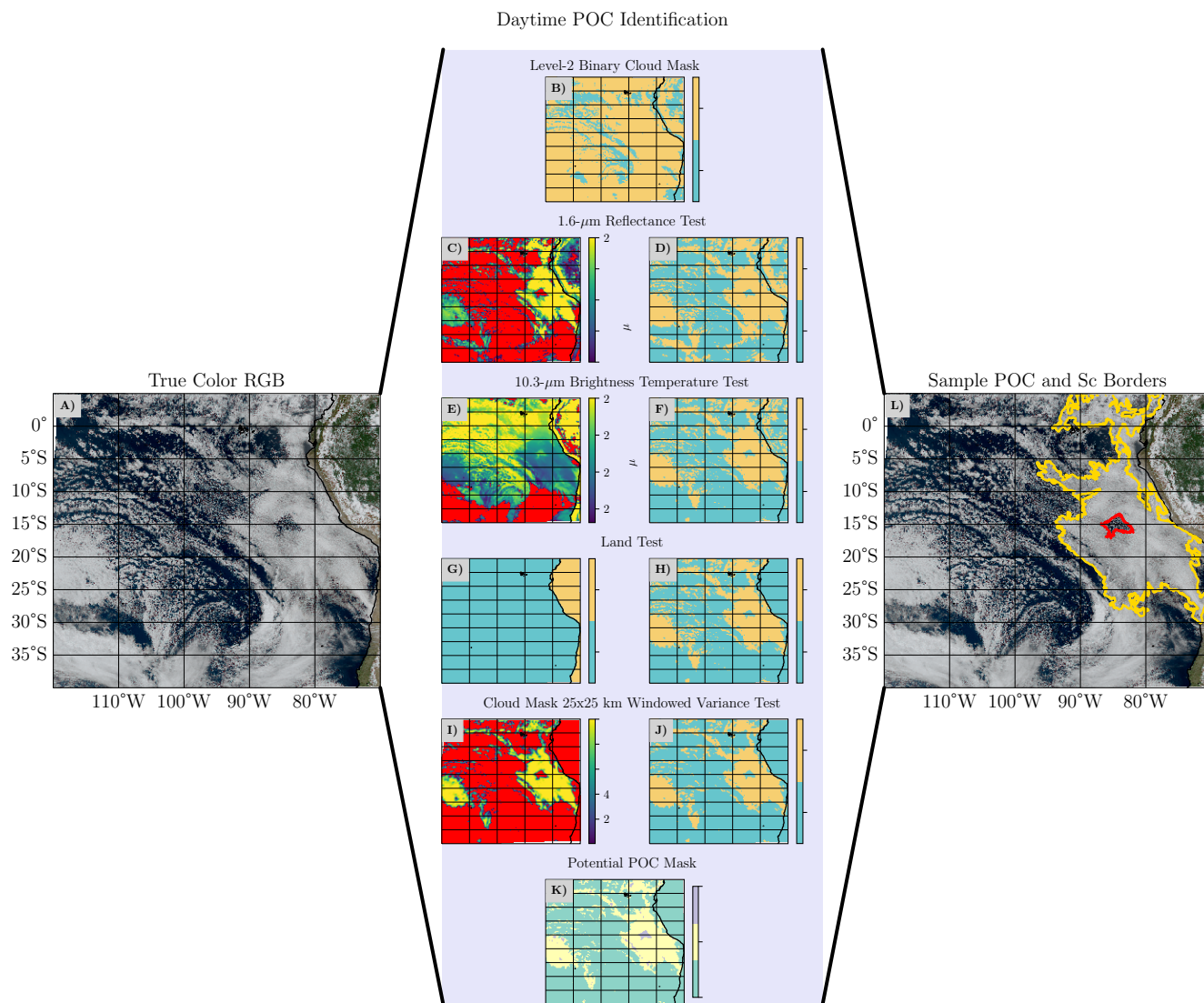


Figure 2. Daytime POC Identification Steps. In the third column, the stratocumulus deck borders are in yellow and POC borders are in red.

To compare closed-cell StCu that develop into POCs and closed-cell StCu that do not, we run additional trajectories initialized at the same starting location of each POC trajectory at ± 24 -hour intervals until we find a CONTROL trajectory that does not intersect any POCs to ensure both the POC and CONTROL trajectories travel through similar meteorological regimes at the same time of day. Using a 24-hour interval between POC and CONTROL trajectories results in 147 of the 258 POCs identified having a valid CONTROL. Similar to the POC trajectories, we define a before, during, and after time for the CONTROL trajectories. Specifically, we define the "before" time as the time prior to the CONTROL trajectory reaching the location where

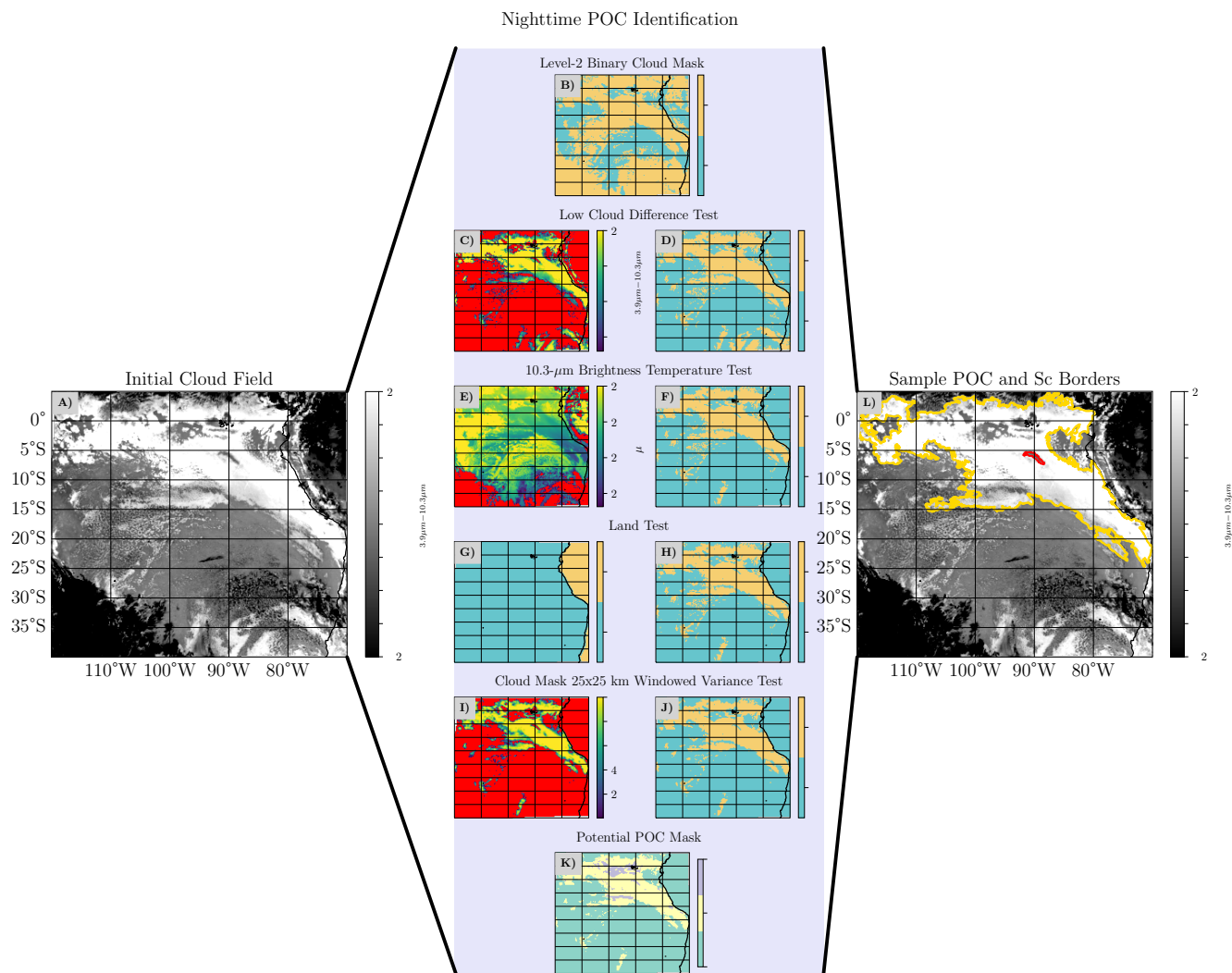


Figure 3. Nighttime POC Identification Steps. In the third column, the stratocumulus deck borders are in yellow and POC borders are in red.

the POC forms, and we define the "after" time as the time after the CONTROL trajectory reaches the location where the POC
 140 dissipates.

2.3 Cloud Properties

We compare the following cloud properties along the POC and CONTROL trajectories: CF, cloud optical depth (COD), cloud
 top effective radius (r_e), liquid water path (LWP), and cloud drop number concentration (N). COD, r_e , LWP, and N are compos-
 145 ited from cloudy pixels within a $0.5^\circ \times 0.5^\circ$ window surrounding each trajectory point because this window size is close to the
 same size as a MERRA-2 gridbox. Finally, CF is defined as the number of cloudy pixels divided by the total number of pixels



within each window. As mentioned prior, different channels and algorithms are used to retrieve COD and r_e during the day and night. During the day, a combination of $0.64\text{-}\mu\text{m}$ and $2.25\text{-}\mu\text{m}$ reflectance are used (Walther et al., 2013), while $3.9\text{-}\mu\text{m}$, $11.2\text{-}\mu\text{m}$, and $12.3\text{-}\mu\text{m}$ brightness temperatures are used at night (Minnis and Heck, 2012). The day/night retrieval algorithms are fundamentally different, therefore the daytime and nighttime cloud properties are separated in the remainder of the paper.

150 At night, COD is limited from 0 to 16 and r_e is limited to $2\ \mu\text{m} - 78\ \mu\text{m}$, whereas, during the day, COD can be retrieved from 0.25 to 158 and r_e can be retrieved from $2\ \mu\text{m}$ to $100\ \mu\text{m}$. The dynamic range is smaller at night because the emissivity of larger particles is similar at $11.2\text{-}\mu\text{m}$ and $12.3\text{-}\mu\text{m}$, resulting in a smaller range of COD and r_e values that can be discerned (Lin and Coakley, 1993). An effect of the limited range of nighttime optical depth retrievals is that a noticeable fraction of nighttime CODs are exactly 16. Finally, any values retrieved during twilight (solar zenith angles from $65^\circ - 90^\circ$) are of degraded quality

155 (Minnis and Heck, 2012; Walther et al., 2013) and are therefore removed resulting in a short diurnal sampling gap in the cloud property data. LWP is derived using equation 8, and N is derived using equation 9 from from (Wood, 2006).

One potential limitation of the data is cirrus contamination. To account for this, we use different sets of tests, that are not used in the POC identification algorithm, during the day and night to remove cirrus. During the day, cirrus removal is based on the GEOS $1.37\text{-}\mu\text{m}$ channel (Schmit et al., 2018), and all cloud-property values within any $0.5^{circ} \times 0.5^{circ}$ window containing

160 any $1.37\text{-}\mu\text{m}$ reflectance values < 5 are removed. We subjectively chose this value, because we visually found a $1.37\text{-}\mu\text{m}$ reflectance threshold of 5 results in the lowest amount of non-cirrus cloud removal, while removing the most cirrus. We also use $8.4\text{-}\mu\text{m} - 10.3\text{-}\mu\text{m}$ brightness temperature difference ($TB_{8.4\mu\text{m}} - TB_{10.3\mu\text{m}}$) to remove cirrus because $TB_{8.4\mu\text{m}} - TB_{10.3\mu\text{m}}$ tends to have positive values for ice clouds and small negative values for low water clouds (Baum et al., 2000; Giannakos and Feidas, 2013); previous studies (Krebs et al., 2007; Strandgren et al., 2017) have removed retrievals with $TB_{8.4\mu\text{m}} - TB_{10.3\mu\text{m}} > -5\ \text{K}$. At

165 night, we use a stricter $TB_{10.3\mu\text{m}} - TB_{3.9\mu\text{m}}$ threshold to remove cirrus based on the assumption that any negative $TB_{10.3\mu\text{m}} - TB_{3.9\mu\text{m}}$ are likely representative of cold clouds (Jedlovec et al., 2008), such that any cloud retrievals with $TB_{10.3\mu\text{m}} - TB_{3.9\mu\text{m}} < 0\ \text{K}$ are removed. This algorithm effectively removes thick cirrus; however, it struggles to remove thin cirrus. Despite this, we find any potential influence of thin cirrus does not affect the overall statistics discussed in our results. Note, these tests are not used to flag cirrus clouds moving over the StCu deck that our POC identification algorithm may identify as a potential POC, because

170 we can visually distinguish cirrus from POCs in the weekly animations.

2.4 Precipitation

We compare precipitation intensity along both the POC and CONTROL trajectories using the Advanced Microwave Scanning Radiometer 2 (AMSAR-2) precipitation product from (Eastman et al., 2019). This dataset is based on statistical relationships between $4 \times 6\ \text{km}^2$ AMSR-E 89 GHz microwave brightness temperatures and collocated CloudSat rain rates, applied to $3 \times 5\ \text{km}^2$

175 AMSR-2 observations. These statistics are used to derive CloudSat-like precipitation across the microwave radiometer swath, which allows for significantly more potential overlap with GOES-16 identified POC cases than does CloudSat. We co-locate AMSR-2 with GOES-16 by identifying any time within 20 minutes of a GOES-16 timestamp where AMSR-2 precipitation is observed within any $0.5^\circ \times 0.5^\circ$ POC box. Figure ??a visually demonstrates this, showing variations in matched precipitation within an example POC. However, due to the statistical nature of the AMSR-2 product, we find that the data identify 98% of



180 all POC and CONTROL AMSR-2 pixels as possibly raining over SEPAC, which is much higher than the typical rain fractions we found of 5% using the rain certain classification from CloudSat. To correct this, we use a precipitation threshold of 0.1 mm day⁻¹, which corresponds to rain probabilities in the AMSR-2 product typically below 5% (Figure ??b) and is consistent with the minimum observable value of surface rain (Comstock et al., 2004; Rapp et al., 2013).

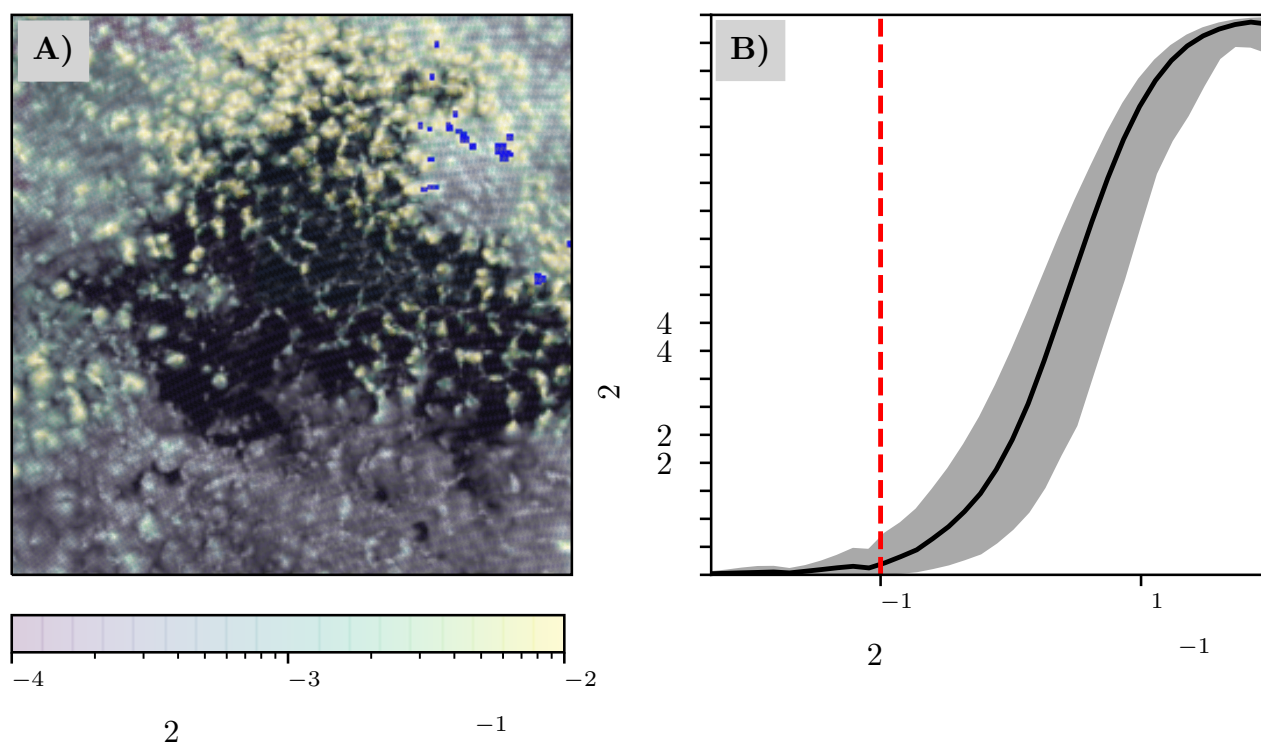


Figure 4. AMSR-2 rain rates matched to the POC shown in Figure 2 overlaid on GOES-16 0.64- μm reflectance are shown in panel A). AMSR-2 rain probability as a function of rain rate for all September-November 2019 data over the entire domain are shown in panel B), where the solid black line represents the median probability at a given rain rate, grey fill represents the 10th-90th percentile spread at a given rain rate, and the dashed red line represents the rain rate threshold of 0.1 mm day⁻¹.

2.5 Environmental Conditions

185 We classify the large-scale environment at each point along the POC and CONTROL trajectories using sea-level pressure (SLP), estimated-inversion strength (EIS), 700-mb water vapor mixing ratio (q_v), 700-mb omega (ω), planetary-boundary layer (PBL) height, PBL mean q_v , lifted condensation level (LCL) height, aerosol-optical depth (AOD), 50-m winds, and 925-mb wind speed/direction, all of which are derived from MERRA-2. EIS is calculated using equation 4 from (Wood and Bretherton, 2006), where lower-tropospheric stability (LTS; Slingo, 1987; Klein and Hartmann, 1993) represents the difference between



190 potential temperature at 700 mb and sea-surface temperature is taken from MERRA-2. The 850-mb moist adiabatic lapse rate
(γ_m^{850}) is derived using Metpy (May and Bruick, 2019). The LCL height is derived using MERRA-2 surface temperature and
the formulation of Romps (2017). MERRA-2 outputs two PBL Height variables, one (PBLH) based on the total-eddy diffusion
coefficient of heat (PBLH), and another based on the bulk Richardson number (TCZPBL; McGrath-Spangler and Molod,
2014). Ding et al. (2021) found both generate PBL depths shallower than those derived directly from satellites, but PBLH is
195 closer. Therefore, we use PBLH as our proxy for PBL height.

3 Results

3.1 General POC Characteristics

Of the 147 POCs that have valid CONTROLS, Figure 5a shows that most POCs traverse between 5°S-25°S, and 80°W-100°W,
similar to prior satellite-based studies (Wood et al., 2008; Watson-Parris et al., 2021). In comparison, Figure 5b shows the
200 CONTROL trajectories take similar paths to the POC trajectories, increasing our confidence that both the POC and CONTROL
trajectories experience similar meteorology during their lifetimes.

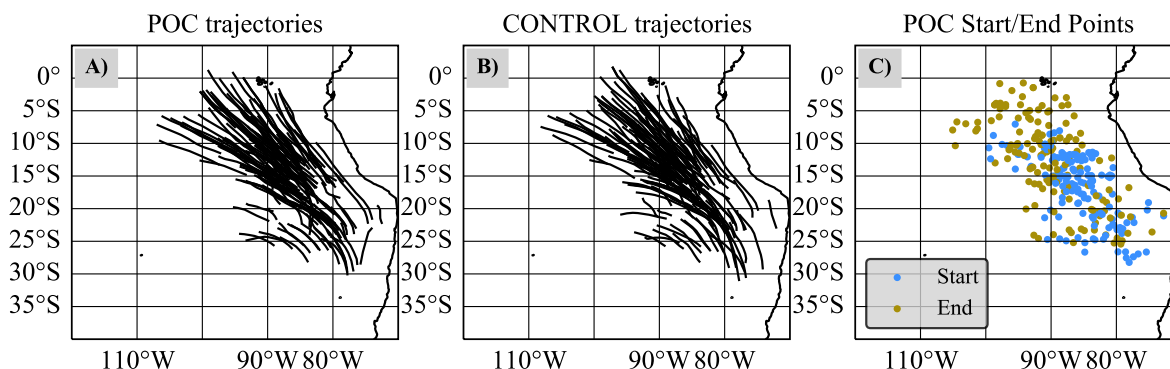


Figure 5. MERRA-2 trajectories that traverse closed-cell stratocumulus and develop into pockets of open cells are shown in panel A), the MERRA trajectories that traverse through closed-cell stratocumulus and never develop into pockets of open cells are shown in panel B), and POC starting and ending points are shown in Panels C).

Interestingly, 88% of all POCs never re-close, meaning that they remain open-celled until they exit typically north/northwest
of the StCu deck. Further breaking this down, 129 POCs never re-close, 12 POCs re-close, and 6 of the calculated trajectories
leave their associated POC area prematurely. Note that the 6 POC trajectories that prematurely exit POCs are not included in
205 the remainder of this analysis. Here we note that we could use the POC centroids themselves to define the trajectory to salvage
these discarded trajectories. However, that method would only work during the POC lifetime whereas the use of reanalysis
trajectories allows us to extend the trajectories both before and after the POC lifetime. Using a cloud-resolving model, Feingold
et al. (2015) found that the recovery from open- to closed-cell StCu is much slower than the transition from closed- to open-cell



Sc, and it depends on the replenishment of aerosols resulting in cloud water increases exceeding precipitation loss. Our results suggest this does not frequently happen in the SEPAC, and as a result, POCs that never re-close and those that do are grouped together throughout the remainder of this paper.

Figure 5c shows the location where POCs typically begin and end, showing that POCs tend to form between 10°S-20°S, and 80°W-90°W and that POC starting locations tend to cluster more than POC ending location. This implies that there is relatively high variability in POC duration. To quantify this, Figure 6 shows a histogram of POC duration. POCs are generally long-lived and last an average of 20 hours, similar to previous observational (Stevens et al., 2005) and modeling (Berner et al., 2013) results.

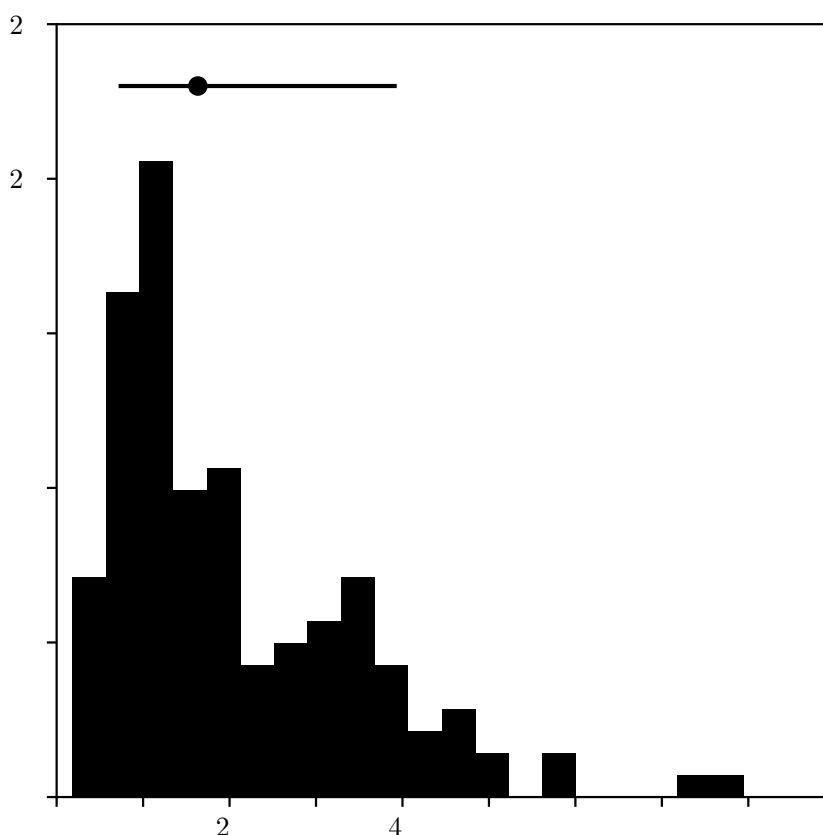


Figure 6. Histogram of POC duration. The black dot above the histogram represents the median and the horizontal black line represents the 10th to 90th percentile spread.

To determine the diurnal cycle in start and end times of POCs, Figure 7 shows the relative frequency of POC start and end times, with POCs typically forming at night and ending during the day. Night time formation is consistent with prior literature that found POC formation is most likely at night when precipitation is most intense and StCu are thickest (Wood et al., 2008;



220 Burleyson et al., 2013). However we find a relatively uniform distribution of start times throughout the night, in contrast to previous results. Why might POCs preferentially end (exit the Sc) during the day? We find that StCu area reaches a minimum around 12 local time (Figure s-1). As a result, we hypothesize that this may simply be the result of a general reduction in StCu extent during the daylight hours (Burleyson and Yuter, 2015), so that the StCu edge effectively moves towards the POC during sunlight.

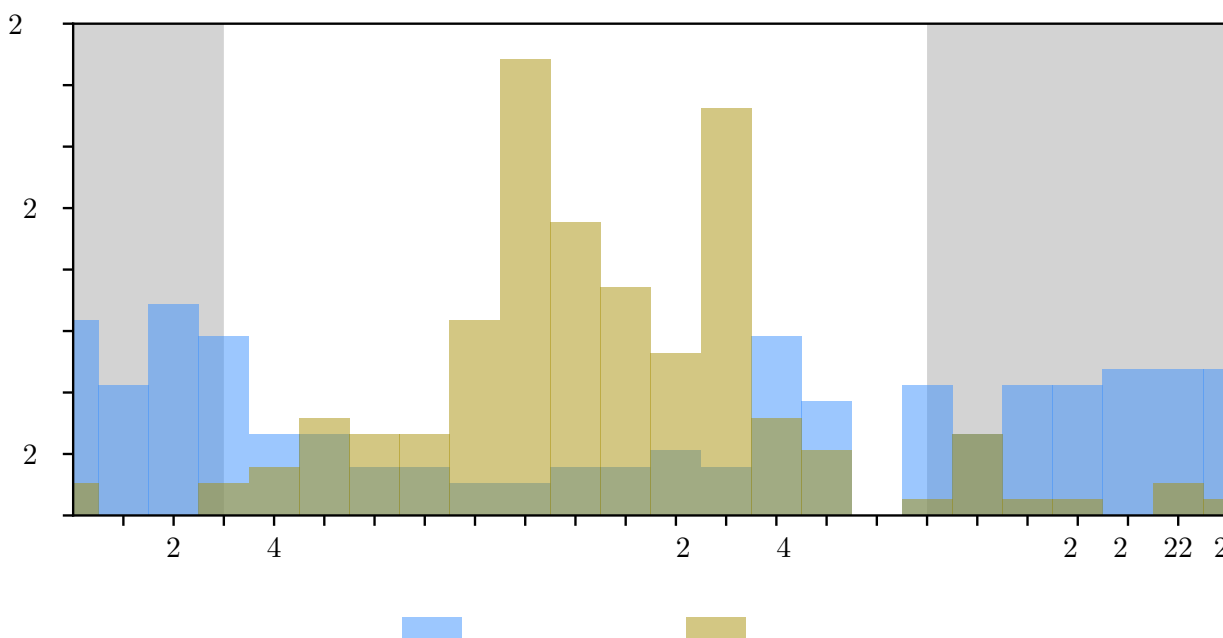


Figure 7. Histograms of POC start time (blue) and end time (brown).

225 Figure 8a shows the relative frequency distributions of the maximum and average POC area. The average POC area is $2.23 \times 10^4 \text{ km}^2$ and reaches a maximum size of $7.13 \times 10^4 \text{ km}^2$, three times larger than most POCs found by Watson-Parris et al. (2021). The differences may result from different algorithm sensitivity or regional sampling differences between the SEPAC and their global statistics. Figure 8b shows changes in POC maximum area as a function of POC duration. POCs tend to grow larger the longer they last, with POCs lasting > 20 hours having a maximum area approximately 10 times larger (3.01×10^5 230 km^2) than those lasting less than 10 hours ($2.69 \times 10^4 \text{ km}^2$).

3.2 POC Occurrence and Associated Environment

In this section the large-scale environmental conditions are contrasted between periods when POCs occur frequently and when they do not occur. For this analysis we include all 258 identified POCs. Figure 11 shows that there are usually between 0 and 7 POCs on any given day. However, this activity is not random, with extended periods of frequent POC occurrence, followed

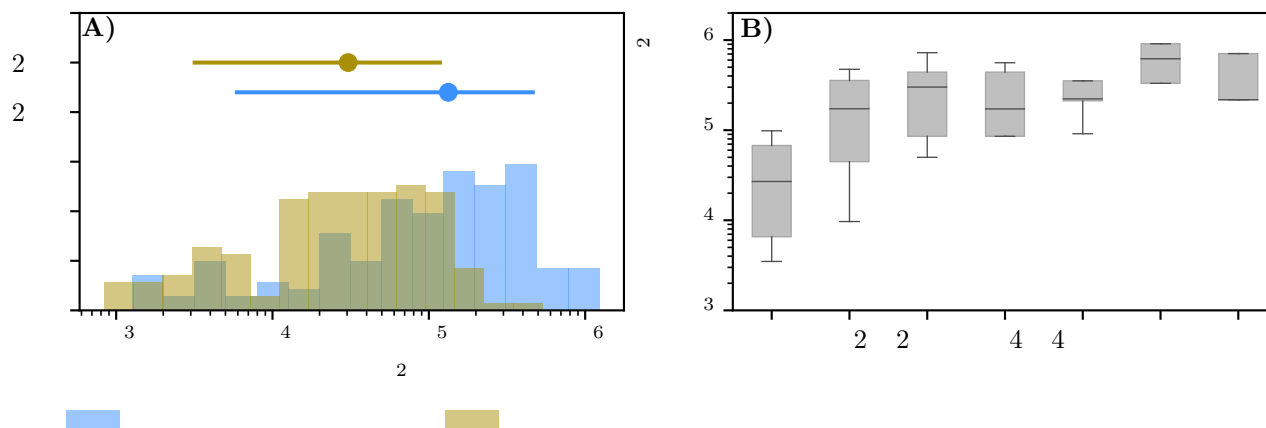


Figure 8. Histograms of POC maximum (blue) and average (brown) area are shown in panel A). The distribution of POC area as a function of POC duration is shown as box plots in panel B), where the solid line represents the median duration, the shaded box represents the interquartile range, and the whiskers represent data between the 10th and 90th percentiles.

235 by sustained periods with few POCs. We find the interquartile range of the daily POC count to be 0 and 7. Therefore, we grouped days when no POCs developed and days when > 7 POCs developed together separately, and composited the average environments for both groups as shown in Figure 10.

Setting the stage synoptically, we find that a surface high pressure system (Figures 10a and 110b) is present south of the geographic maximum low-CFs in both cases. On average, SLP is moderately lower during periods when the most POCs develop (Figure 10c), resulting in weaker southeasterly winds (Figure 10f) in the region of highest StCu CF. In both cases, there is a strong inversion with EIS typically > 5 K (Figures 10p and 10q) and the presence of lower-free-tropospheric subsidence (Figures 10s and 10t) which are conducive to StCu clouds. Interestingly, EIS is stronger over the southern part of the SEPAC but weaker where most POCs begin (Figure 10r).

On days with the most POCs, the PBL is on average shallower (Figure 10i), moister (Figure 10l), and with a lower LCL (Figure 10o). The lowering of PBL and LCL height have similar patterns and magnitudes suggesting a relatively constant cloud layer depth between POC and non-POC days. Figure 10x shows AOD is generally lower, except very close to the continent, on days with the most POCs. This is consistent with prior studies that found POC air tends to be cleaner than non-POC air (e.g. Wood et al., 2011; Terai et al., 2014). However, the pattern of the composite difference is still complicated and we must exercise some caution in the interpretation of an aerosol field derived from a reanalysis.

250 On days with the most POCs, a shallower and moister boundary layer, lower LCLs, large-scale subsidence, and a strong inversion promotes higher low-CFs (Wood, 2012) and larger StCu area (Figure 11). As a result, a simple explanation for why

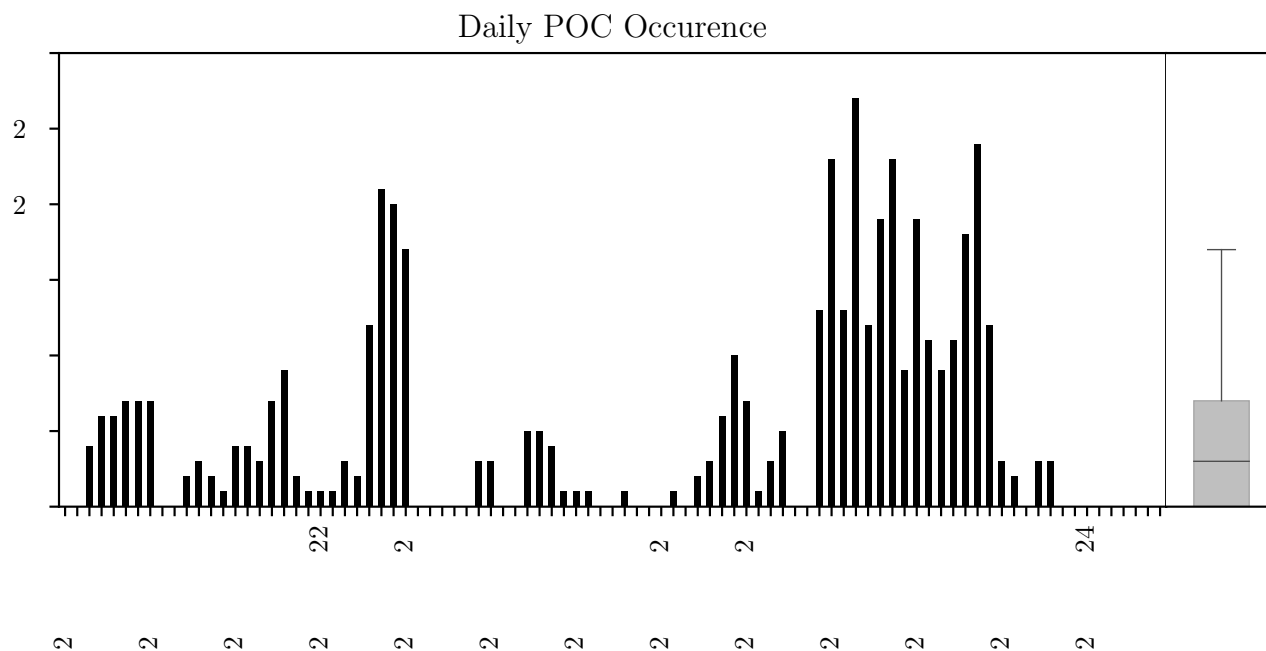


Figure 9. The number of POCs occurring on each day is shown. The boxplot represents the overall distribution of daily POC occurrence, where the solid line represents the median duration, the shaded box represents the interquartile range, and the whiskers represent data between the 10th and 90th percentiles.

there are several days with no POCs and several days with many may be that environmental conditions more favorable for StCu development result in a higher likelihood of POC development.

3.3 Cloud-Field Characteristics

255 We now turn to a comparison of CF and cloud microphysical properties for the POC and CONTROL cases. Figure 12 shows the evolution of example POC and CONTROL trajectories in terms of CF, average COD, average in-cloud LWP, average r_e , and average N. The largest changes along the POC trajectory are in CF, COD, r_e , and N relative to the CONTROL trajectory, while LWP remains relatively constant. Specifically, Figure 12a shows that CF decreases as the POC develops. This decrease in CF is accompanied by decreasing COD (Figure 12b), increasing effective radius (Figure 12d), and decreasing N (Figure 12e). These
260 variables then remain relatively constant during the POC's lifetime before approaching pre-POC values after POC dissipation. Larger r_e and lower N inside of this non-re-closing POC is consistent with the development of precipitation, resulting in the closed- to open-cell transition (Comstock et al., 2007; Savic-Jovicic and Stevens, 2008; Wang et al., 2010b; Glassmeier and Feingold, 2017).

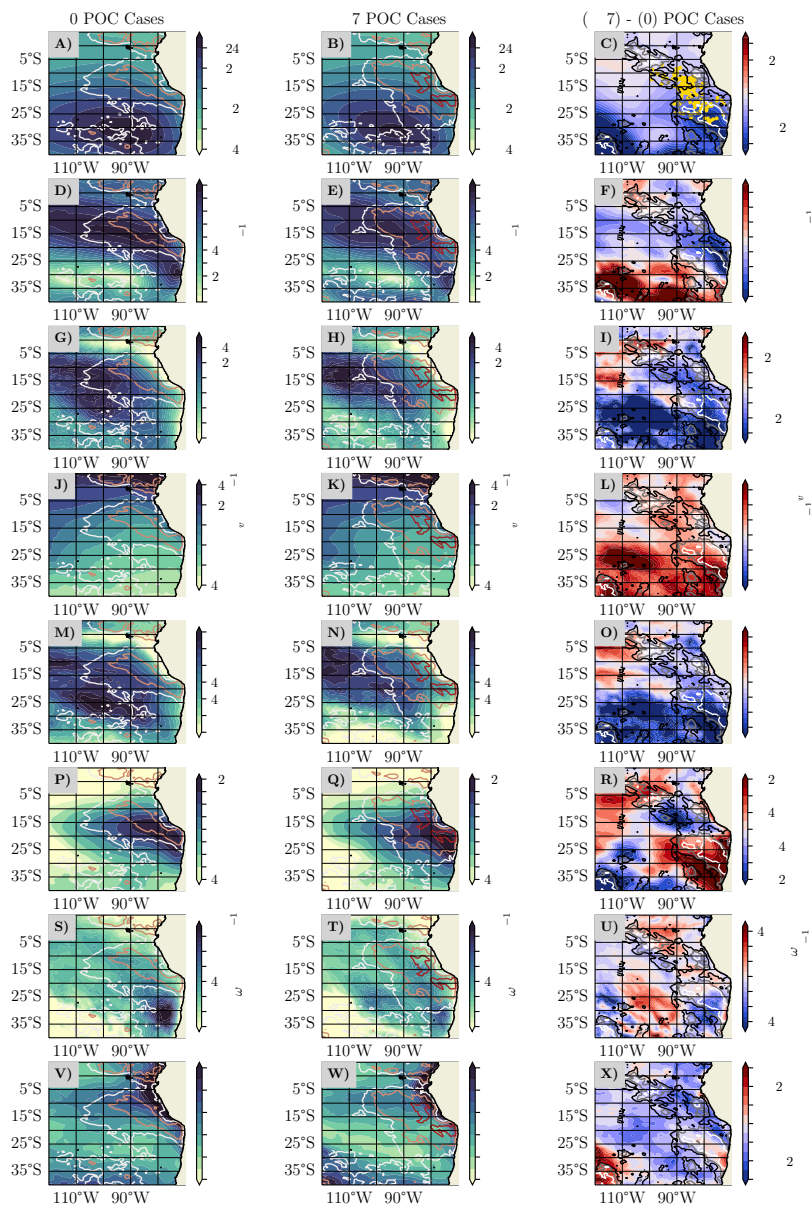


Figure 10. Average sea-level pressure (SLP; panel A), 50-m winds (panel D), planetary-boundary layer (PBL) height (panel G), average PBL water vapor mixing ratio (q_v ; panel J), lifted-condensation level (LCL; panel M), estimated-inversion strength (EIS; panel P), 700-mb omega (ω ; panel S), and total-column aerosol-optical depth (AOD; panel V) are shown in the first column for days when no POCs occur. The second column shows the same variables for days when > 7 POCs occur. The third panel shows the difference between each variable for days with > 7 POCs and days with no POCs. The non-filled contours overlaid in all panels represent cloud fraction, where white represents 70%, orange represents 80%, and red represents 90%. The gold dots shown in panel C overlay POC starting point.

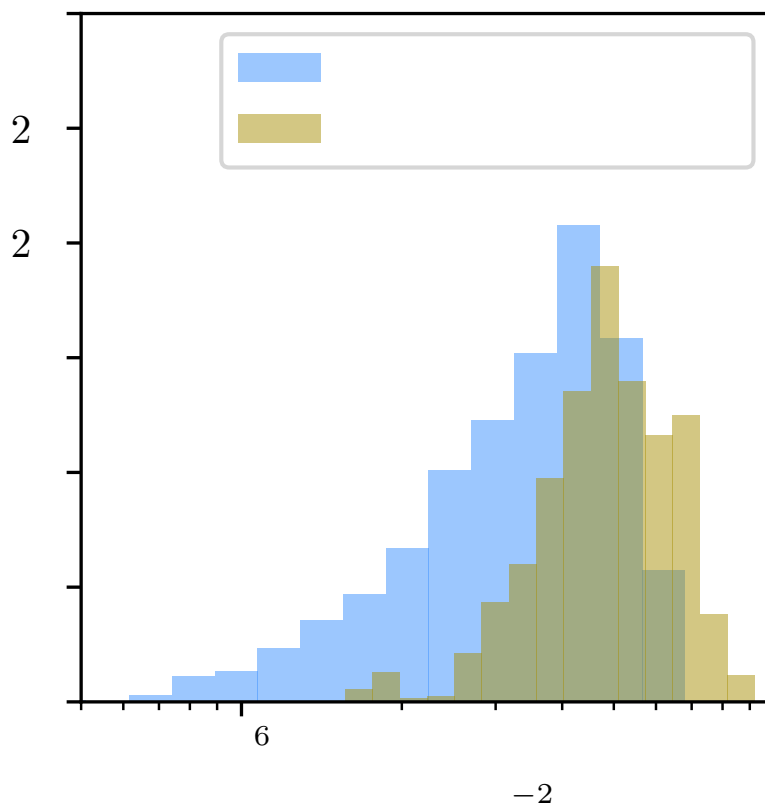


Figure 11. Distributions of stratocumulus area for days with no POCs (blue) and days with > 7 POCs (brown) are shown above.

One case gives us a glimpse at how cloud field properties vary throughout a POC's lifetime, and how they compare to a
265 CONTROL case. However, more cases are needed to make more definitive conclusions. Therefore, we composite all the cloud
field properties for all POC cases and their corresponding CONTROL case, and we then compare the distribution of each
variable before POC formation, during POC lifetime, and after POC dissipation. We then separate daytime and nighttime data
because the retrieval algorithms are subject to very different sensitivity and uncertainty limitations.

Figure 13 shows the 10^{th} - 90^{th} percentile spread (see Figure S2 for the full daytime distributions) in the cloud field and
270 precipitation characteristics of all POCs and their associated CONTROL trajectory. For all POC cases during the day, CF and
COD are similar to the CONTROL cases before POC formation. There are indications of elevated LWP, r_e and N relative to
the CONTROL trajectory before POC formation suggesting drizzle initiation before a visible cloud regime transition. Once
the POCs form, CF decreases, COD decreases, LWP decreases, r_e increases, and N decreases for all POC cases relative to the
CONTROL cases. However, LWP remains similar to the CONTROL cases for the POC cases during POC lifetime.

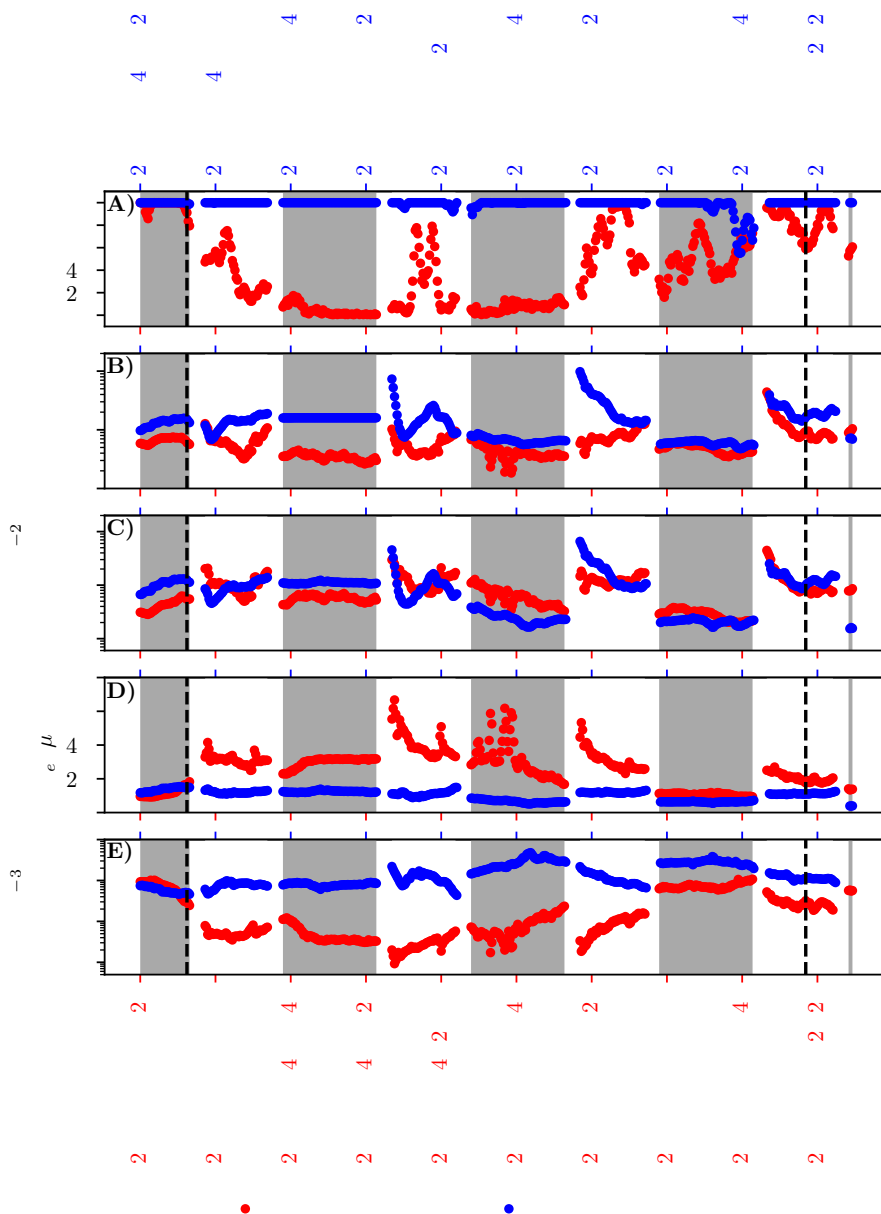


Figure 12. : Changes in cloud fraction (panel A), cloud optical depth (panel B), liquid water path (panel C), effective radius (panel D), and cloud drop number concentration (panel E) are shown along the trajectory for a sample POC case that occurred between 09/03/2019 and 09/07/2019. The purple dots correspond to the sample POC trajectory, while the green dots correspond to the corresponding CONTROL trajectory. Gray shading indicates night time periods.

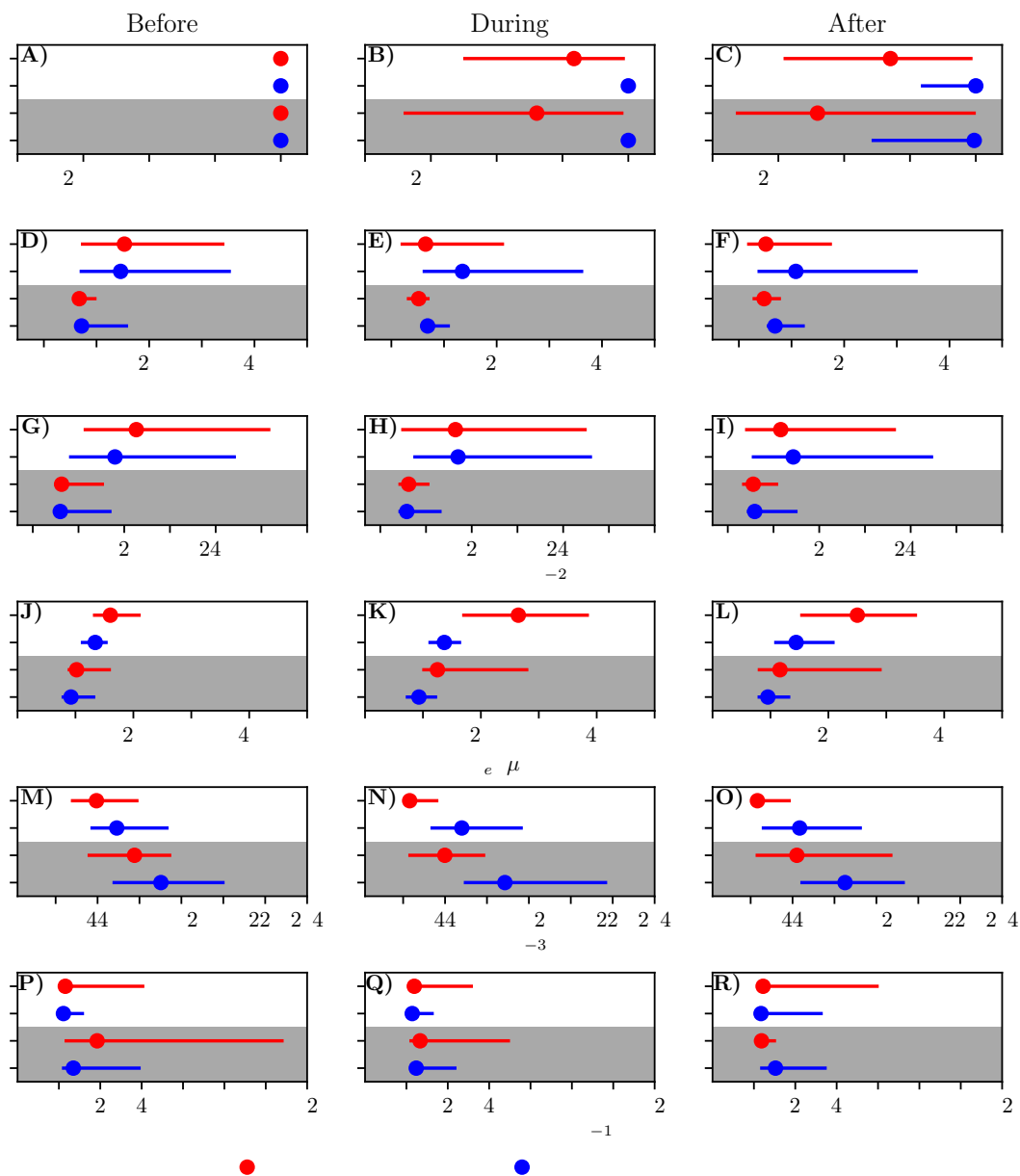


Figure 13. Daytime statistics for cloud fraction (A, B, and C), cloud-optical depth (D, E, and f), liquid-water path (G, H, and I), cloud-top effective radius (J, K, and L), cloud-drop number concentration (M, N, and O), and AMSR-2 rain rate (P, Q, and R) are shown in the upper-white half of each panel, while the nighttime statistics are shown in the grey-lower half of each panel. Red values represent the POC trajectories, while the blue values represent the CONTROL trajectories. The colored dots represent the median of each distribution, and the horizontal lines represent the spread between the 10th and 90th percentiles.



275 Switching to the nighttime data, Figure 13 (see Figure S3 for the full nighttime distributions) shows that the overall patterns in CF, COD, r_e , and N and how they compare to the CONTROL cases are similar to the daytime characteristics of all POCs, with one main difference. The COD and derived LWP are substantially smaller than in the daytime data, and the CONTROL and POC LWP are essentially indistinguishable at night. This is likely an artifact of the limited dynamic range of the GOES-16 nighttime algorithms. Nevertheless, given the substantial algorithmic differences in retrieved COD and r_e at night versus during
280 the day, it is encouraging that the microphysical patterns (i.e. r_e and N) are similar. In particular, one might be concerned that the daytime differences between the POC and CONTROL trajectories are merely an artifact of 3D radiative transfer artifacts differentially affecting the two regimes (Zhang et al., 2012; Liang et al., 2015). However, the fact that these signals are also observed in the emission-based nighttime data lends credence to their sign, while uncertainty in their magnitude remains.

3.4 Precipitation Characteristics

285 Figures 13p-r show the precipitation statistics in a manner similar to the cloud statistics. To further illustrate the differences between POC and CONTROL precipitation, Figure 14 shows the distribution of rate-weighted rain rate. Specifically, each bin is multiplied by bin-center rain rate, which places a higher weight on bins with more intense rainfall such that the area under the histogram is equal to the accumulated rainfall.

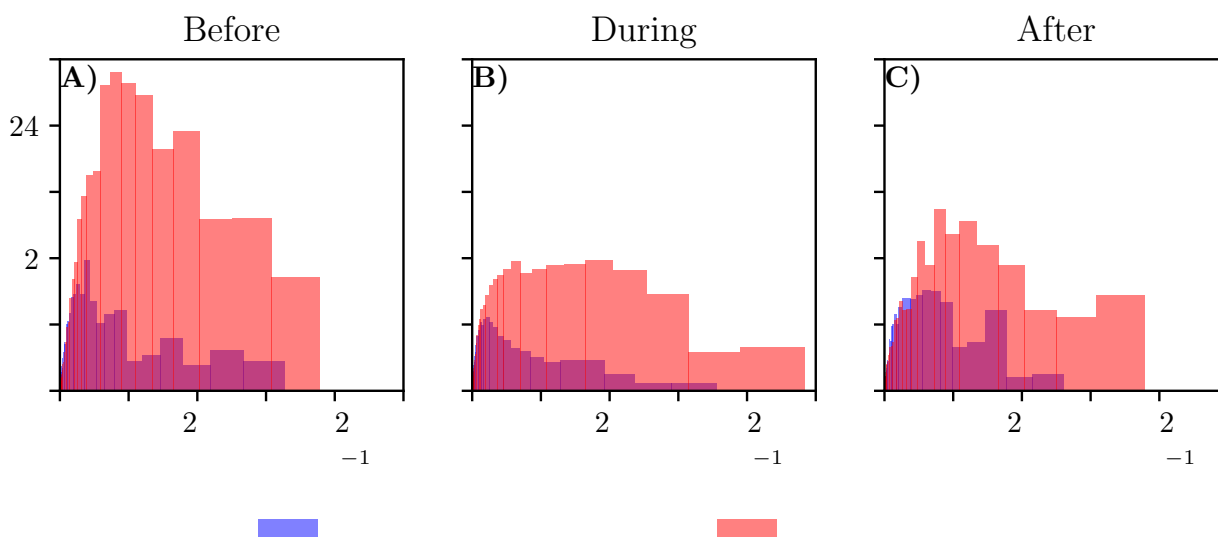


Figure 14. Histograms of rain rate along the POC (red) and CONTROL (blue) trajectories before (A), during (b), and after (c) POC lifetime are shown, where each bin is multiplied by bin-center rain rate (e.g. accumulation weighted) and the area under each curve is normalized to mean rain rate for each distribution



Precipitation rates are typically low with median values between 0.14 and 0.44 mm day^{-1} and they remain relatively constant from before POC development until after POC dissipation. Precipitation is generally more intense at night than during the day (Figure 13p-r) which is consistent with prior works (Wood et al., 2008; Burleyson et al., 2013). Notably, there is a larger spread in rain rate, with more frequent intense precipitation for the POC cases compared to the CONTROL cases. Although evident during both day and night, the differences in the occurrence of the most intense precipitation between the POC and CONTROL cases are most distinct before POC development at night. Furthermore, Figure 14 clearly highlights that there is substantially more precipitation accumulation for POC than control trajectories during the POC lifetime. Together these findings are consistent with larger re (Figures 13j-l) and lower N (Figures 13m-o) retrieved from GOES-16 for POCs than controls, which suggest that intensity and quantity of precipitation is key to the formation and maintenance of POCs.

3.5 Environmental Characteristics

In section 3.2, we evaluated the synoptic environment during periods of frequent POC occurrence and rare occurrence in an attempt to identify conditions conducive to POC formation. Most notably we found that the largest numbers of POCs tended to form when AOD is low and the StCu area is high. Here we will instead evaluate the differences in the environmental conditions along the POC trajectories with the CONTROLS to identify whether there are systematic differences between the large-scale forcing experienced by the two trajectories. We focus primarily on PBL characteristics because of their potential importance of rain to POC development. We find that PBL height (Figures 15a-c), mean moisture (Figures 15d-f), LCL height (Figures 15g-i), AOD (Figures 15j-l), and PBL winds (Figure 16) are similar for both the POC and CONTROL cases, with PBL height around 800 - 1400 m, moisture around 7 - 11 g kg^{-1} , AOD around 0.05 - 0.15 , LCL height around 400 - 600 m, and winds from the southeast at 20 knots. Additionally, we find there are no significant differences between the POC and CONTROL cases in EIS, $700\text{-mb } q_v$, and $700\text{-mb } \omega$ (Figure s-4). Holistically, these results are consistent with the expectation that few differences exist between large-scale forcing where POCs form and those where they do not. This implies that the process relevant to the formation and maintenance of POCs are small-scale processes within the PBL.

4 Summary and Discussion

This study develops a novel methodology to identify POCs and then uses a Lagrangian analysis to track their evolution and how that compares to CONTROL trajectories of closed-cell StCu that never transition. Along the trajectories, we analyze the cloud field characteristics, and environmental characteristics of both cases. We find that POCs tend to last on average 20 hours, have a maximum area larger than 104 km^2 , and exit the StCu deck without re-closing 88% of the time.

We find that POC development and maintenance are most highly correlated with processes that influence cloud microphysical state such as precipitation (Wood et al., 2011; Burleyson et al., 2013; Burleyson and Yuter, 2015; Eastman et al., 2021) as opposed to large-scale forcing, which does not appear to have an impact on POC formation (Sharon et al., 2006; Bretherton et al., 2010; Berner et al., 2011, 2013). Modeling studies (Feingold et al., 2010; Yamaguchi and Feingold, 2015) have inferred that POC formation may be related to the clustering of raining closed-cell StCu that drives the development of interacting cold

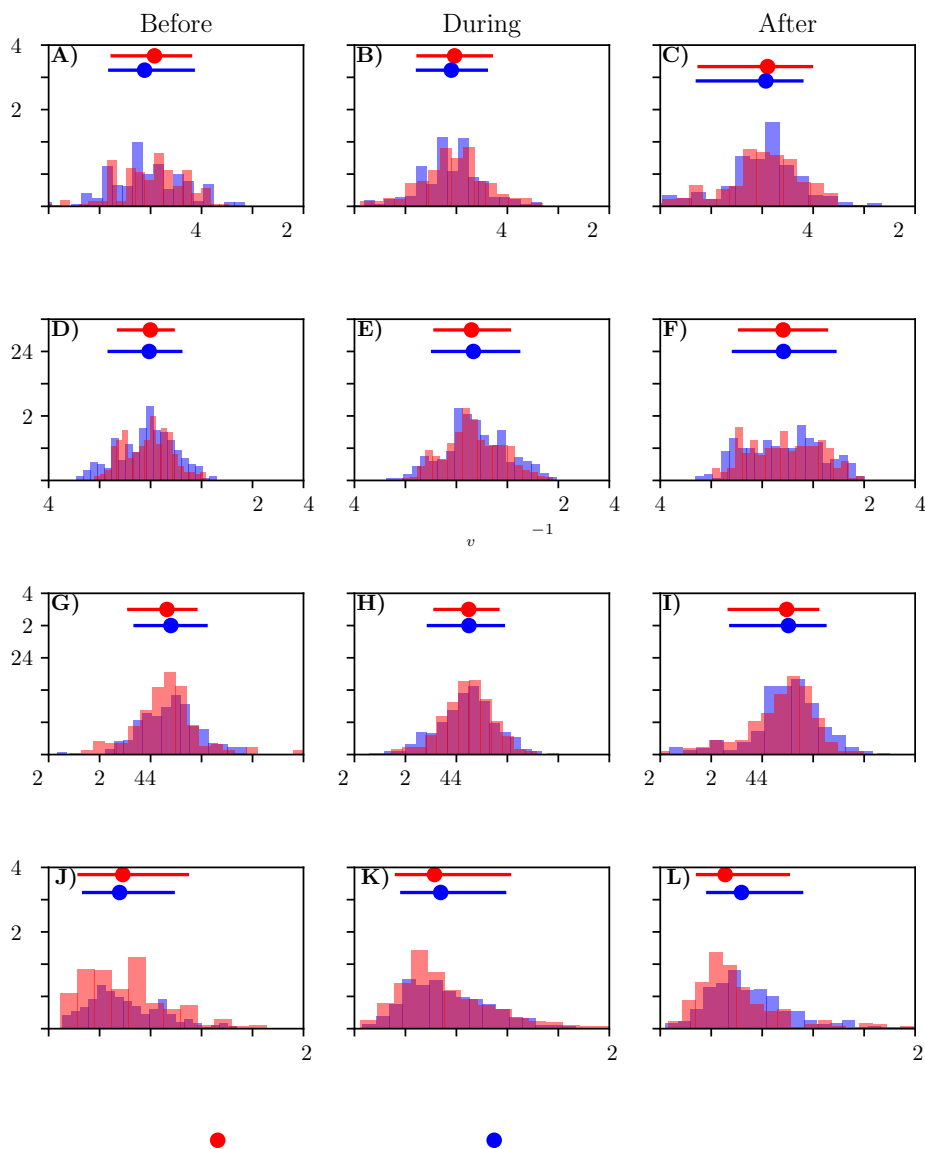


Figure 15. Distributions of environmental properties before a POC forms (left column), during POC lifetime (middle), and after POC dissipation (right). Top row (A, B, and C) shows planetary boundary layer (PBL) height. PBL-average water vapor mixing ratio q_v is shown in the second row (D, E, and F). Lifted-condensation level height is shown in the third row (G, H, and I). Aerosol optical depth is shown in the fourth row (J, K, and L). Red represents distributions mapped to the POC trajectories, while blue represents the distributions mapped to the CONTROL trajectories. The colored dots represent the median of each distribution, and the horizontal lines represent spread between the 10th and 90th percentiles.

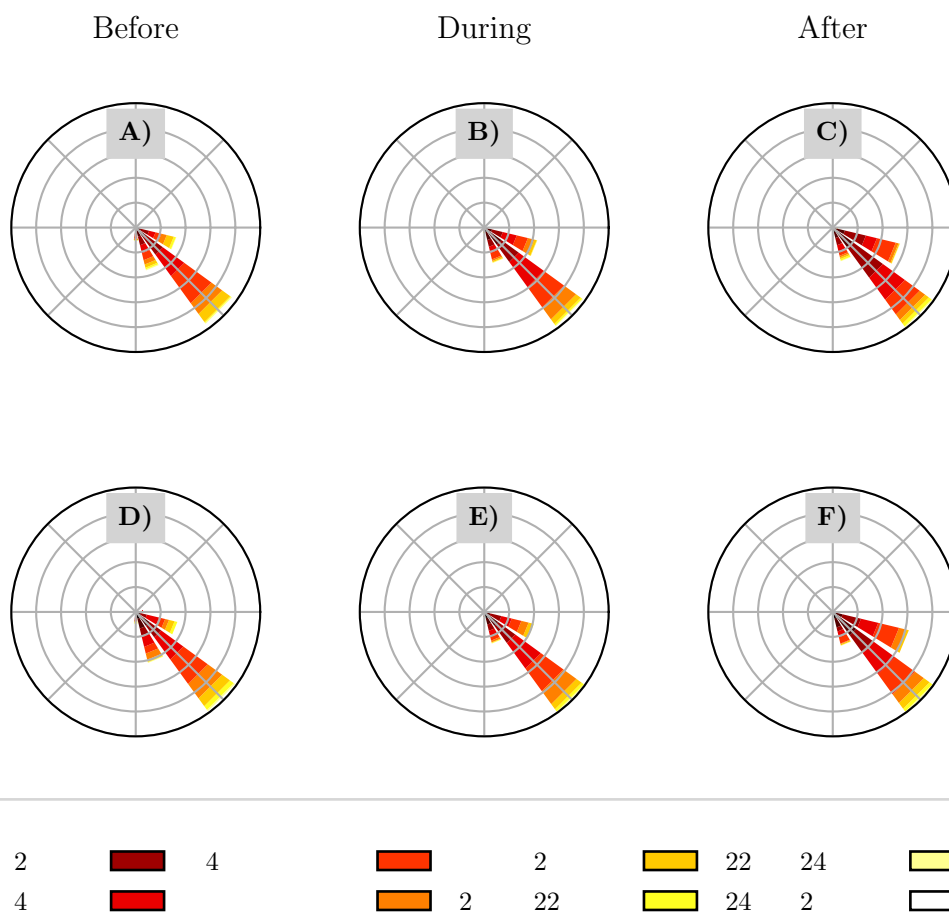


Figure 16. Wind rose plots are used to show the most common 925-mb wind speed and direction before a POC (panels A and D), during a POC (panels B and E), and after a POC ends (panels C and F). The wind rose plots in the top row represent the trajectories that intersect a POC, while those in the bottom row represent the trajectories that do not intersect a POC.

325 pools, which subsequently causes more intense precipitation and initiates the transition to open cells. Even though we cannot observe changes in precipitation organization alone from GOES-16, our results show that r_e is typically higher, N is lower, more precipitation falls and is more intense for POCs than the CONTROL population before POC formation. These findings are consistent with precipitation occurrence and intensity driving likely cold-pool development and subsequent reductions in CF. Yamaguchi and Feingold (2015) used a cloud-resolving model to show that the distance between precipitating StCu cells is important to open-cell development. After POC formation our results show that more frequent rain persists, while effective radius becomes even larger and N decreases further than before POC formation. It is, however, also possible that at least



some of the observed increases in effective radius during the POC period could be related to retrieval artifacts associated with increasing sub-pixel heterogeneity (Zhang et al., 2012; Liang et al., 2015).

330 Overall, these results appear robust and suggest precipitation as a key driver of POC development. However, we found evidence, similar to Allen et al. (2013), suggesting gravity waves may also influence POC development. We found this happened infrequently over SEPAC during September–November, 2019. Therefore, more observations over a longer timeframe are needed to assess their influence.

The general understanding of broader StCu to cumulus transitions is that they occur when StCu drift over warmer sea surfaces, leading to deeper and decoupled boundary layers (Albrecht et al., 1995; Wyant et al., 1997; Bretherton and Wyant, 1997; Stevens, 2000; Wood and Bretherton, 2004), in which cumulus clouds begin to develop that penetrate the overlying StCu layer and mix drier free-tropospheric air into the cloud layer (e.g. Wyant et al., 1997). These studies have argued that precipitation is not necessary for these transitions to occur, however there has been some debate over the importance of precipitation in the timing of the transition (e.g. Paluch and Lenschow, 1991; Yamaguchi et al., 2015; Eastman and Wood, 2016; de Roode et al., 2016; Yamaguchi et al., 2017). Considering most POCs identified in this study never re-close, our results suggest that the development of POCs driven by organizing precipitation can mediate the timing of the stratocumulus to cumulus transition. Yamaguchi et al. (2017) used LES to investigate the influence of precipitation on StCu transitions, finding that, when aerosol/drop number concentrations are low due to precipitation, the StCu transition can be rapidly accelerated. Additionally, as the open-cells within POCs continue to organize and precipitation intensity increases, the StCu deck transitions to a precipitating shallow cumulus field (Yamaguchi et al., 2017). These results may explain why most POC cases we observe never re-close, but more observational studies tracking POCs over a longer timeframe and across more regions are needed to draw more general conclusions.

The results herein have important implications for aerosol–cloud–interactions and climate change mitigation through marine cloud brightening. Importantly, current models do a poor job of representing the warm rain process (e.g. Sun et al., 2006; Kharin et al., 2007; Wehner et al., 2014; Christopoulos and Schneider, 2021; Witte et al., 2021) and the scavenging effect of precipitation on aerosol (e.g. Tost et al., 2010; Grandey et al., 2014; Gettelman et al., 2015; Michibata et al., 2019; Jing et al., 2019). Our finding that POCs tend to accelerate the StCu – cumulus transition and not to reclose suggests that the ability of aerosol to enhance cloud albedo is highly dependent on the current state of the cloud field. Specifically, the efficiency of cloud condensation nuclei at influencing cloud albedo over the cloud lifetime would be maximized prior to the nascent formation of drizzle that precedes POC development.

Even though our analysis is limited to a 3-month period over the SEPAC and may not generalize to other marine stratocumulus-dominated regions of the globe (i.e., northeast Pacific and southeast Atlantic basins). We believe, most importantly, that this study demonstrates that the improved spatio-temporal resolution of the current generation of geostationary sensors and the associated data product suite provides an important tool in evaluating the temporal dimension of POCs for future studies.



360 *Code availability.* Please contact the authors for access to any dataset created by the analysis and/or the code used to process the GOES-16/AMSR-2 data..

Data availability. The GOES-16 level-1 and level-2 data are available at <https://registry.opendata.aws/noaa-goes/>.

Author contributions. KS performed the analysis presented in this paper. RE provided the AMSR-2 precipitation data. KS prepared the paper with contributions from ML, RE, MS, and MW.

365 *Competing interests.* The authors declare that they have no conflict of interest.

Acknowledgements. This work was performed at the Jet Propulsion Laboratory, California Institute of Technology, under a contract with the National Aeronautics and Space Administration and was funded by the CloudSat mission. MKW was supported in part by the US Department of Energy's Atmospheric System Research, an Office of Science Biological and Environmental Research program, under Grant No. DE-SC0020332. We thank Dr. Rob Wood for several helpful discussions.



370 References

- Abel, S. J., Boutle, I. A., Waite, K., Fox, S., Brown, P. R. A., Cotton, R., Lloyd, G., Choulaton, T. W., and Bower, K. N.: The Role of Precipitation in Controlling the Transition from Stratocumulus to Cumulus Clouds in a Northern Hemisphere Cold-Air Outbreak, *Journal of the Atmospheric Sciences*, 74, <https://doi.org/10.1175/JAS-D-16-0362.1>, 2017.
- Abel, S. J., Barrett, P. A., Zuidema, P., Zhang, J., Christensen, M., Peers, F., Taylor, J. W., Crawford, I., Bower, K. N., and Flynn, M.: Open
375 cells exhibit weaker entrainment of free-tropospheric biomass burning aerosol into the south-east Atlantic boundary layer, *Atmospheric Chemistry and Physics*, 20, <https://doi.org/10.5194/acp-20-4059-2020>, 2020.
- Albrecht, B. A., Bretherton, C. S., Johnson, D., Scubert, W. H., and Frisch, A. S.: The Atlantic Stratocumulus Transition Experiment—ASTEX, *Bulletin of the American Meteorological Society*, 76, [https://doi.org/10.1175/1520-0477\(1995\)076<0889:TASTE>2.0.CO;2](https://doi.org/10.1175/1520-0477(1995)076<0889:TASTE>2.0.CO;2), 1995.
- 380 Allen, G., Vaughan, G., Toniazzo, T., Coe, H., Connolly, P., Yuter, S. E., Burleyson, C. D., Minnis, P., and Ayers, J. K.: Gravity-wave-induced perturbations in marine stratocumulus, *Quarterly Journal of the Royal Meteorological Society*, 139, <https://doi.org/10.1002/qj.1952>, 2013.
- Aminou, D. M. A.: MSG's SEVIRI Instrument, Tech. rep., European Space Research and Technology Centre, 2002.
- Austin, P., Wang, Y., Kujala, V., and Pincus, R.: Precipitation in Stratocumulus Clouds: Observational and Modeling Results, *Journal of the Atmospheric Sciences*, 52, 2329–2352, [https://doi.org/10.1175/1520-0469\(1995\)052<2329:PISCOA>2.0.CO;2](https://doi.org/10.1175/1520-0469(1995)052<2329:PISCOA>2.0.CO;2), 1995.
- 385 Baum, B. A., Soulen, P. F., Strabala, K. I., King, M. D., Ackerman, S. A., Menzel, W. P., and Yang, P.: Remote sensing of cloud properties using MODIS airborne simulator imagery during SUCCESS: 2. Cloud thermodynamic phase, *Journal of Geophysical Research Atmospheres*, 105, <https://doi.org/10.1029/1999JD901090>, 2000.
- Berner, A. H., Bretherton, C. S., and Wood, R.: Large-eddy simulation of mesoscale dynamics and entrainment around a pocket of open cells observed in VOCALS-REx RF06, *Atmospheric Chemistry and Physics*, 11, <https://doi.org/10.5194/acp-11-10525-2011>, 2011.
- 390 Berner, A. H., Bretherton, C. S., Wood, R., and Muhlbauer, A.: Marine boundary layer cloud regimes and POC formation in a CRM coupled to a bulk aerosol scheme, *Atmospheric Chemistry and Physics*, 13, <https://doi.org/10.5194/acp-13-12549-2013>, 2013.
- Bretherton, C. S. and Wyant, M. C.: Moisture Transport, Lower-Tropospheric Stability, and Decoupling of Cloud-Topped Boundary Layers, *Journal of the Atmospheric Sciences*, 54, [https://doi.org/10.1175/1520-0469\(1997\)054<0148:MTL TSA>2.0.CO;2](https://doi.org/10.1175/1520-0469(1997)054<0148:MTL TSA>2.0.CO;2), 1997.
- Bretherton, C. S., Uttal, T., Fairall, C. W., Yuter, S. E., Weller, R. A., Baumgardner, D., Comstock, K., Wood, R., and Raga, G. B.: The Epic
395 2001 Stratocumulus Study, *Bulletin of the American Meteorological Society*, 85, <https://doi.org/10.1175/BAMS-85-7-967>, 2004.
- Bretherton, C. S., Uchida, J., and Blossey, P. N.: Slow Manifolds and Multiple Equilibria in Stratocumulus-Capped Boundary Layers, *Journal of Advances in Modeling Earth Systems*, 2, <https://doi.org/10.3894/JAMES.2010.2.14>, 2010.
- Burleyson, C. D. and Yuter, S. E.: Patterns of Diurnal Marine Stratocumulus Cloud Fraction Variability*, *Journal of Applied Meteorology and Climatology*, 54, 847–866, <https://doi.org/10.1175/JAMC-D-14-0178.1>, 2015.
- 400 Burleyson, C. D., de Szoek, S. P., Yuter, S. E., Wilbanks, M., and Brewer, W. A.: Ship-Based Observations of the Diurnal Cycle of Southeast Pacific Marine Stratocumulus Clouds and Precipitation, *Journal of the Atmospheric Sciences*, 70, 3876–3894, <https://doi.org/10.1175/JAS-D-13-01.1>, 2013.
- Christopoulos, C. and Schneider, T.: Assessing Biases and Climate Implications of the Diurnal Precipitation Cycle in Climate Models, *Geophysical Research Letters*, 48, e2021GL093017, <https://doi.org/10.1029/2021GL093017>, e2021GL093017
405 2021GL093017, 2021.



- Comstock, K. K., Wood, R., Yuter, S. E., and Bretherton, C. S.: Reflectivity and rain rate in and below drizzling stratocumulus, *Quarterly Journal of the Royal Meteorological Society*, 130, 2891–2918, <https://doi.org/https://doi.org/10.1256/qj.03.187>, 2004.
- Comstock, K. K., Bretherton, C. S., and Yuter, S. E.: Mesoscale Variability and Drizzle in Southeast Pacific Stratocumulus, *Journal of the Atmospheric Sciences*, 62, <https://doi.org/10.1175/JAS3567.1>, 2005.
- 410 Comstock, K. K., Yuter, S. E., Wood, R., and Bretherton, C. S.: The Three-Dimensional Structure and Kinematics of Drizzling Stratocumulus, *Monthly Weather Review*, 135, <https://doi.org/10.1175/2007MWR1944.1>, 2007.
- de Roode, S. R., Sandu, I., van der Dussen, J. J., Ackerman, A. S., Blossey, P., Jarecka, D., Lock, A., Siebesma, A. P., and Stevens, B.: Large-Eddy Simulations of EUCLIPSE–GASS Lagrangian Stratocumulus-to-Cumulus Transitions: Mean State, Turbulence, and Decoupling, *Journal of the Atmospheric Sciences*, 73, <https://doi.org/10.1175/JAS-D-15-0215.1>, 2016.
- 415 Ding, F., Iredell, L., Theobald, M., Wei, J., and Meyer, D.: PBL Height From AIRS, GPS RO, and MERRA-2 Products in NASA GES DISC and Their 10-Year Seasonal Mean Intercomparison, *Earth and Space Science*, 8, e2021EA001859, <https://doi.org/https://doi.org/10.1029/2021EA001859>, e2021EA001859 2021EA001859, 2021.
- Eastman, R. and Wood, R.: Factors Controlling Low-Cloud Evolution over the Eastern Subtropical Oceans: A Lagrangian Perspective Using the A-Train Satellites, *Journal of the Atmospheric Sciences*, 73, <https://doi.org/10.1175/JAS-D-15-0193.1>, 2016.
- 420 Eastman, R., Lebsock, M., and Wood, R.: Warm Rain Rates from AMSR-E 89-GHz Brightness Temperatures Trained Using CloudSat Rain-Rate Observations, *Journal of Atmospheric and Oceanic Technology*, 36, <https://doi.org/10.1175/JTECH-D-18-0185.1>, 2019.
- Eastman, R., McCoy, I. L., and Wood, R.: Environmental and internal controls on Lagrangian transitions from closed cell mesoscale cellular convection over subtropical oceans, *Journal of the Atmospheric Sciences*, <https://doi.org/10.1175/JAS-D-20-0277.1>, 2021.
- Feingold, G., Koren, I., Wang, H., Xue, H., and Brewer, W. A.: Precipitation-generated oscillations in open cellular cloud fields, *Nature*, 466, 425 849–852, <https://doi.org/10.1038/nature09314>, 2010.
- Feingold, G., Koren, I., Yamaguchi, T., and Kazil, J.: On the reversibility of transitions between closed and open cellular convection, *Atmospheric Chemistry and Physics*, 15, <https://doi.org/10.5194/acp-15-7351-2015>, 2015.
- Gelaro, R., McCarty, W., Suárez, M. J., Todling, R., Molod, A., Takacs, L., Randles, C. A., Darmenov, A., Bosilovich, M. G., Reichle, R., Wargan, K., Coy, L., Cullather, R., Draper, C., Akella, S., Buchard, V., Conaty, A., da Silva, A. M., Gu, W., Kim, G.-K., Koster, R., Lucchesi, R., Merkova, D., Nielsen, J. E., Partyka, G., Pawson, S., Putman, W., Rienecker, M., Schubert, S. D., Sienkiewicz, M., and Zhao, B.: The Modern-Era Retrospective Analysis for Research and Applications, Version 2 (MERRA-2), *Journal of Climate*, 30, <https://doi.org/10.1175/JCLI-D-16-0758.1>, 2017.
- 430 Gattelman, A., Morrison, H., Santos, S., Bogenschutz, P., and Caldwell, P. M.: Advanced Two-Moment Bulk Microphysics for Global Models. Part II: Global Model Solutions and Aerosol?Cloud Interactions, *Journal of Climate*, 28, 1288 – 1307, <https://doi.org/10.1175/JCLI-D-14-00103.1>, 2015.
- Ghate, V. P., Cadetdu, M. P., and Wood, R.: Drizzle, Turbulence, and Density Currents Below Post Cold Frontal Open Cellular Marine Stratocumulus Clouds, *Journal of Geophysical Research: Atmospheres*, 125, <https://doi.org/10.1029/2019JD031586>, 2020.
- Giannakos, A. and Feidas, H.: Classification of convective and stratiform rain based on the spectral and textural features of Meteosat Second Generation infrared data, *Theoretical and Applied Climatology*, 113, <https://doi.org/10.1007/s00704-012-0802-z>, 2013.
- 440 Glassmeier, F. and Feingold, G.: Network approach to patterns in stratocumulus clouds, *Proceedings of the National Academy of Sciences*, 114, <https://doi.org/10.1073/pnas.1706495114>, 2017.



- Goren, T., Rosenfeld, D., Sourdeval, O., and Quaas, J.: Satellite Observations of Precipitating Marine Stratocumulus Show Greater Cloud Fraction for Decoupled Clouds in Comparison to Coupled Clouds, *Geophysical Research Letters*, 45, <https://doi.org/10.1029/2018GL078122>, 2018.
- 445 Grandey, B. S., Gururaj, A., Stier, P., and Wagner, T. M.: Rainfall-aerosol relationships explained by wet scavenging and humidity, *Geophysical Research Letters*, 41, 5678–5684, <https://doi.org/https://doi.org/10.1002/2014GL060958>, 2014.
- Gupta, S., McFarquhar, G. M., O'Brien, J. R., Delene, D. J., Poellot, M. R., Dobracki, A., Podolske, J. R., Redemann, J., LeBlanc, S. E., Segal-Rozenhaimer, M., and Pistone, K.: Impact of the variability in vertical separation between biomass burning aerosols and marine stratocumulus on cloud microphysical properties over the Southeast Atlantic, *Atmospheric Chemistry and Physics*, 21, [https://doi.org/10.5194/acp-](https://doi.org/10.5194/acp-21-4615-2021)
450 21-4615-2021, 2021.
- Hastings, D. A. and Dunbar, P. K.: Global Land One-kilometer Base Elevation (GLOBE) Digital Elevation Model, Documentation, Volume 1.0. Key to Geophysical Records Documentation (KGRD), Tech. rep., National Oceanic and Atmospheric Administration, National Geophysical Data Center, 325 Broadway, Boulder, Colorado 80303, U.S.A., 1999.
- Heidinger, A. and Straka, W. C.: NOAA NESDIS CENTER for SATELLITE APPLICATIONS and RESEARCH ALGORITHM THEORETICAL BASIS DOCUMENT ABI Cloud Mask, Tech. rep., NOAA NESDIS Center for Satellite Application and Research,
455 <https://www.goes-r.gov/products/baseline-clear-sky-mask.html>, 2012.
- Hunt, G. E.: Radiative properties of terrestrial clouds at visible and infra-red thermal window wavelengths, *Quarterly Journal of the Royal Meteorological Society*, 99, <https://doi.org/10.1002/qj.49709942013>, 1973.
- Jedlovec, G., Haines, S., and LaFontaine, F.: Spatial and Temporal Varying Thresholds for Cloud Detection in GOES Imagery, *IEEE Transactions on Geoscience and Remote Sensing*, 46, <https://doi.org/10.1109/TGRS.2008.916208>, 2008.
- Jing, X., Suzuki, K., and Michibata, T.: The Key Role of Warm Rain Parameterization in Determining the Aerosol Indirect Effect in a Global Climate Model, *Journal of Climate*, 32, 4409 – 4430, <https://doi.org/10.1175/JCLI-D-18-0789.1>, 2019.
- Khari, V. V., Zwiers, F. W., Zhang, X., and Hegerl, G. C.: Changes in Temperature and Precipitation Extremes in the IPCC Ensemble of Global Coupled Model Simulations, *Journal of Climate*, 20, 1419 – 1444, <https://doi.org/10.1175/JCLI4066.1>, 2007.
- 465 Klein, S. A. and Hartmann, D. L.: The seasonal cycle of low stratiform clouds, *Journal of Climate*, 6, [https://doi.org/10.1175/1520-0442\(1993\)006<1587:TSCOLS>2.0.CO;2](https://doi.org/10.1175/1520-0442(1993)006<1587:TSCOLS>2.0.CO;2), 1993.
- Krebs, W., Mannstein, H., Bugliaro, L., and Mayer, B.: Technical note: A new day- and night-time Meteosat Second Generation Cirrus Detection Algorithm MeCiDA, *Atmospheric Chemistry and Physics*, 7, <https://doi.org/10.5194/acp-7-6145-2007>, 2007.
- Liang, L., Di Girolamo, L., and Sun, W.: Bias in MODIS cloud drop effective radius for oceanic water clouds as deduced
470 from optical thickness variability across scattering angles, *Journal of Geophysical Research: Atmospheres*, 120, 7661–7681, <https://doi.org/https://doi.org/10.1002/2015JD023256>, 2015.
- Lin, X. and Coakley, J. A.: Retrieval of properties for semitransparent clouds from multispectral infrared imagery data, *Journal of Geophysical Research*, 98, <https://doi.org/10.1029/93jd01793>, 1993.
- May, R. and Bruick, Z.: MetPy: An Community-Driven, Open-Source Python Toolkit for Meteorology, in: AGU Fall Meeting Abstracts, vol. 2019, pp. NS21A–16, 2019.
- 475 McCoy, I. L., Wood, R., and Fletcher, J. K.: Identifying Meteorological Controls on Open and Closed Mesoscale Cellular Convection Associated with Marine Cold Air Outbreaks, *Journal of Geophysical Research: Atmospheres*, 122, 11,678–11,702, <https://doi.org/10.1002/2017JD027031>, 2017.



- 480 McGrath-Spangler, E. L. and Molod, A.: Comparison of GEOS-5 AGCM planetary boundary layer depths computed with various definitions, *Atmospheric Chemistry and Physics*, 14, 6717–6727, <https://doi.org/10.5194/acp-14-6717-2014>, 2014.
- Michibata, T., Suzuki, K., Sekiguchi, M., and Takemura, T.: Prognostic Precipitation in the MIROC6-SPRINTARS GCM: Description and Evaluation Against Satellite Observations, *Journal of Advances in Modeling Earth Systems*, 11, 839–860, <https://doi.org/https://doi.org/10.1029/2018MS001596>, 2019.
- 485 Miller, S. D., Noh, Y. J., and Heidinger, A. K.: Liquid-top mixed-phase cloud detection from shortwave-infrared satellite radiometer observations: A physical basis, *Journal of Geophysical Research*, 119, 8245–8267, <https://doi.org/10.1002/2013JD021262>, 2014.
- Minnis, P. and Heck, P.: NOAA NESDIS CENTER for SATELLITE APPLICATIONS and RESEARCH GOES-R Advanced Baseline Imager (ABI) Algorithm Theoretical Basis Document For Nighttime Cloud Optical Depth, Cloud Particle Size, Cloud Ice Water Path, and Cloud Liquid Water Path, Tech. rep., NOAA NESDIS CENTER for SATELLITE APPLICATIONS and RESEARCH, <https://www.goes-r.gov/products/baseline-cloud-opt-depth.html>, 2012.
- 490 Painemal, D. and Zuidema, P.: Microphysical variability in southeast Pacific Stratocumulus clouds: synoptic conditions and radiative response, *Atmospheric Chemistry and Physics*, 10, <https://doi.org/10.5194/acp-10-6255-2010>, 2010.
- Paluch, I. R. and Lenschow, D. H.: Stratiform Cloud Formation in the Marine Boundary Layer, *Journal of the Atmospheric Sciences*, 48, [https://doi.org/10.1175/1520-0469\(1991\)048<2141:SCFITM>2.0.CO;2](https://doi.org/10.1175/1520-0469(1991)048<2141:SCFITM>2.0.CO;2), 1991.
- Petters, M. D., Snider, J. R., Stevens, B., Vali, G., Faloona, I., and Russell, L. M.: Accumulation mode aerosol, pockets of open cells, and particle nucleation in the remote subtropical Pacific marine boundary layer, *Journal of Geophysical Research Atmospheres*, 111, <https://doi.org/10.1029/2004JD005694>, 2006.
- 495 Rapp, A. D., Lebsock, M., and L'Ecuyer, T.: Low cloud precipitation climatology in the southeastern Pacific marine stratocumulus region using CloudSat, *Environmental Research Letters*, 8, 014 027, <https://doi.org/10.1088/1748-9326/8/1/014027>, 2013.
- Raspaud, M., Hoese, D., Dybbroe, A., Lahtinen, P., Devasthale, A., Itkin, M., Hamann, U., Ørum Rasmussen, L., Nielsen, E. S., Lep-
500 pelt, T., Maul, A., Kliche, C., and Thorsteinsson, H.: TOOLS: PyTroll: An open-source, community-driven python framework to process earth observation satellite data, *Bulletin of the American Meteorological Society*, 99, https://doi.org/10.1175/BAMS_997_1313-1336_NOWCAST, 2018.
- Romps, D. M.: Exact expression for the lifting condensation level, *Journal of the Atmospheric Sciences*, 74, <https://doi.org/10.1175/JAS-D-17-0102.1>, 2017.
- 505 Rosenfeld, D., Kaufman, Y. J., and Koren, I.: Switching cloud cover and dynamical regimes from open to closed Benard cells in response to the suppression of precipitation by aerosols, *Atmospheric Chemistry and Physics*, 6, <https://doi.org/10.5194/acp-6-2503-2006>, 2006.
- Sarkar, M., Zuidema, P., Albrecht, B., Ghate, V., Jensen, J., Mohrmann, J., and Wood, R.: Observations Pertaining to Precipitation within the Northeast Pacific Stratocumulus-to-Cumulus Transition, *Monthly Weather Review*, 148, <https://doi.org/10.1175/MWR-D-19-0235.1>, 2019.
- 510 Savic-Jovicic, V. and Stevens, B.: The Structure and Mesoscale Organization of Precipitating Stratocumulus, *Journal of the Atmospheric Sciences*, 65, <https://doi.org/10.1175/2007JAS2456.1>, 2008.
- Schmit, T. J., Griffith, P., Gunshor, M. M., Daniels, J. M., Goodman, S. J., and Lehair, W. J.: A closer look at the ABI on the goes-r series, *Bulletin of the American Meteorological Society*, 98, <https://doi.org/10.1175/BAMS-D-15-00230.1>, 2017.
- Schmit, T. J., Lindstrom, S. S., Gerth, J. J., and Gunshor, M. M.: Applications of the 16 spectral bands on the Advanced Baseline Imager
515 (ABI), *Journal of Operational Meteorology*, 06, 33–46, <https://doi.org/10.15191/nwajom.2018.0604>, 2018.



- Sharon, T. M., Albrecht, B. A., Jonsson, H. H., Minnis, P., Khaiyer, M. M., van Reken, T. M., Seinfeld, J., and Flagan, R.: Aerosol and Cloud Microphysical Characteristics of Rifts and Gradients in Maritime Stratocumulus Clouds, *Journal of the Atmospheric Sciences*, 63, <https://doi.org/10.1175/JAS3667.1>, 2006.
- Slingo, J. M.: The Development and Verification of A Cloud Prediction Scheme For the Ecmwf Model, *Quarterly Journal of the Royal Meteorological Society*, 113, <https://doi.org/10.1002/qj.49711347710>, 1987.
- 520 Stevens, B.: Cloud transitions and decoupling in shear-free stratocumulus-topped boundary layers, *Geophysical Research Letters*, 27, <https://doi.org/10.1029/1999GL011257>, 2000.
- Stevens, B., Vali, G., Comstock, K., Wood, R., van Zanten, M. C., Austin, P. H., Bretherton, C. S., and Lenschow, D. H.: POCKETS OF OPEN CELLS AND DRIZZLE IN MARINE STRATOCUMULUS, *Bulletin of the American Meteorological Society*, 86, 51–58, <https://doi.org/10.1175/BAMS-86-1-51>, 2005.
- 525 Strandgren, J., Bugliaro, L., Sehnke, F., and Schröder, L.: Cirrus cloud retrieval with MSG/SEVIRI using artificial neural networks, *Atmospheric Measurement Techniques*, 10, <https://doi.org/10.5194/amt-10-3547-2017>, 2017.
- Sun, Y., Solomon, S., Dai, A., and Portmann, R. W.: How Often Does It Rain?, *Journal of Climate*, 19, 916 – 934, <https://doi.org/10.1175/JCLI3672.1>, 2006.
- 530 Szoeke, S. P. D., Fairall, C. W., and Pezoa, S.: Ship observations of the tropical Pacific Ocean along the coast of South America, *Journal of Climate*, 22, <https://doi.org/10.1175/2008JCLI2555.1>, 2009.
- Terai, C. R. and Wood, R.: Aircraft observations of cold pools under marine stratocumulus, *Atmospheric Chemistry and Physics*, 13, 9899–9914, <https://doi.org/10.5194/acp-13-9899-2013>, 2013.
- Terai, C. R., Bretherton, C. S., Wood, R., and Painter, G.: Aircraft observations of aerosol, cloud, precipitation, and boundary layer properties in pockets of open cells over the southeast Pacific, *Atmospheric Chemistry and Physics*, 14, <https://doi.org/10.5194/acp-14-8071-2014>, 2014.
- 535 Tost, H., Lawrence, M. G., Brühl, C., Jöckel, P., Team, T. G., and Team, T. S.-O.-D.: Uncertainties in atmospheric chemistry modelling due to convection parameterisations and subsequent scavenging, *Atmospheric Chemistry and Physics*, 10, 1931–1951, <https://doi.org/10.5194/acp-10-1931-2010>, 2010.
- 540 Walther, A., Straka, W., and Heidinger, A. K.: NOAA NESDIS CENTER for SATELLITE APPLICATIONS and RESEARCH ABI Algorithm Theoretical Basis Document For Daytime Cloud Optical and Microphysical Properties (DCOMP), Tech. rep., NOAA NESDIS CENTER for SATELLITE APPLICATIONS and RESEARCH, <https://www.goes-r.gov/products/baseline-cloud-opt-depth.html>, 2013.
- Wang, H. and Feingold, G.: Modeling Mesoscale Cellular Structures and Drizzle in Marine Stratocumulus. Part I: Impact of Drizzle on the Formation and Evolution of Open Cells, *Journal of the Atmospheric Sciences*, 66, <https://doi.org/10.1175/2009JAS3022.1>, 2009.
- 545 Wang, H., Feingold, G., Wood, R., and Kazil, J.: Modelling microphysical and meteorological controls on precipitation and cloud cellular structures in Southeast Pacific stratocumulus, *Atmospheric Chemistry and Physics*, 10, <https://doi.org/10.5194/acp-10-6347-2010>, 2010a.
- Wang, H., Feingold, G., Wood, R., and Kazil, J.: Modelling microphysical and meteorological controls on precipitation and cloud cellular structures in Southeast Pacific stratocumulus, *Atmospheric Chemistry and Physics*, 10, <https://doi.org/10.5194/acp-10-6347-2010>, 2010b.
- 550 Watson-Parris, D., Sutherland, S. A., Christensen, M. W., Eastman, R., and Stier, P.: A Large-Scale Analysis of Pockets of Open Cells and Their Radiative Impact, *Geophysical Research Letters*, 48, e2020GL092213, <https://doi.org/https://doi.org/10.1029/2020GL092213>, e2020GL092213 2020GL092213, 2021.



- Wehner, M. F., Reed, K. A., Li, F., Prabhat, Bacmeister, J., Chen, C.-T., Paciorek, C., Gleckler, P. J., Sperber, K. R., Collins, W. D., Gettelman, A., and Jablonowski, C.: The effect of horizontal resolution on simulation quality in the Community Atmospheric Model, CAM5.1, *Journal of Advances in Modeling Earth Systems*, 6, 980–997, <https://doi.org/10.1002/2013MS000276>, 2014.
- 555 Witte, M. K., Morrison, H., Davis, A. B., and Teixeira, J.: Limitations of bin and bulk microphysics in reproducing the observed spatial structure of light precipitation, *Journal of the Atmospheric Sciences*, <https://doi.org/10.1175/JAS-D-21-0134.1>, 2021.
- Wolters, E. L. A., Deneke, H. M., van den Hurk, B. J. J. M., Meirink, J. F., and Roebeling, R. A.: Broken and inhomogeneous cloud impact on satellite cloud particle effective radius and cloud-phase retrievals, *Journal of Geophysical Research*, 115, <https://doi.org/10.1029/2009JD012205>, 2010.
- 560 Wood, R.: Relationships between optical depth, liquid water path, droplet concentration and effective radius in an adiabatic layer cloud, Tech. rep., University of Washington, https://atmos.uw.edu/~robwood/papers/chilean_plume/optical_depth_relations.pdf, 2006.
- Wood, R.: Stratocumulus Clouds, *Monthly Weather Review*, 140, 2373 – 2423, <https://doi.org/10.1175/MWR-D-11-00121.1>, 2012.
- Wood, R. and Bretherton, C. S.: Boundary Layer Depth, Entrainment, and Decoupling in the Cloud-Capped Subtropical and Tropical Marine Boundary Layer, *Journal of Climate*, 17, [https://doi.org/10.1175/1520-0442\(2004\)017<3576:BLDEAD>2.0.CO;2](https://doi.org/10.1175/1520-0442(2004)017<3576:BLDEAD>2.0.CO;2), 2004.
- 565 Wood, R. and Bretherton, C. S.: On the relationship between stratiform low cloud cover and lower-tropospheric stability, *Journal of Climate*, 19, <https://doi.org/10.1175/JCLI3988.1>, 2006.
- Wood, R., Comstock, K. K., Bretherton, C. S., Cornish, C., Tomlinson, J., Collins, D. R., and Fairall, C.: Open cellular structure in marine stratocumulus sheets, *Journal of Geophysical Research: Atmospheres*, 113, <https://doi.org/10.1029/2007JD009371>, 2008.
- Wood, R., Bretherton, C. S., Leon, D., Clarke, A. D., Zuidema, P., Allen, G., and Coe, H.: An aircraft case study of the spatial
570 transition from closed to open mesoscale cellular convection over the Southeast Pacific, *Atmospheric Chemistry and Physics*, 11, <https://doi.org/10.5194/acp-11-2341-2011>, 2011.
- Wyant, M. C., Bretherton, C. S., Rand, H. A., and Stevens, D. E.: Numerical Simulations and a Conceptual Model of the Stratocumulus to Trade Cumulus Transition, *Journal of the Atmospheric Sciences*, 54, [https://doi.org/10.1175/1520-0469\(1997\)054<0168:NSAACM>2.0.CO;2](https://doi.org/10.1175/1520-0469(1997)054<0168:NSAACM>2.0.CO;2), 1997.
- 575 Yamaguchi, T. and Feingold, G.: On the relationship between open cellular convective cloud patterns and the spatial distribution of precipitation, *Atmospheric Chemistry and Physics*, 15, 1237–1251, <https://doi.org/10.5194/acp-15-1237-2015>, 2015.
- Yamaguchi, T., Feingold, G., Kazil, J., and McComiskey, A.: Stratocumulus to cumulus transition in the presence of elevated smoke layers, *Geophysical Research Letters*, 42, <https://doi.org/10.1002/2015GL066544>, 2015.
- Yamaguchi, T., Feingold, G., and Kazil, J.: Stratocumulus to Cumulus Transition by Drizzle, *Journal of Advances in Modeling Earth Systems*,
580 9, <https://doi.org/10.1002/2017MS001104>, 2017.
- Zhang, Z., Ackerman, A. S., Feingold, G., Platnick, S., Pincus, R., and Xue, H.: Effects of cloud horizontal inhomogeneity and drizzle on remote sensing of cloud droplet effective radius: Case studies based on large-eddy simulations, *Journal of Geophysical Research: Atmospheres*, 117, <https://doi.org/10.1029/2012JD017655>, 2012.
- Zinner, T. and Mayer, B.: Remote sensing of stratocumulus clouds: Uncertainties and biases due to inhomogeneity, *Journal of Geophysical
585 Research*, 111, <https://doi.org/10.1029/2005JD006955>, 2006.